Cell Reports
Physical Science

CellPress
OPEN ACCESS

Article

Intrinsic and extrinsic stability of triple-cation perovskite solar cells through synergistic influence of organic additive

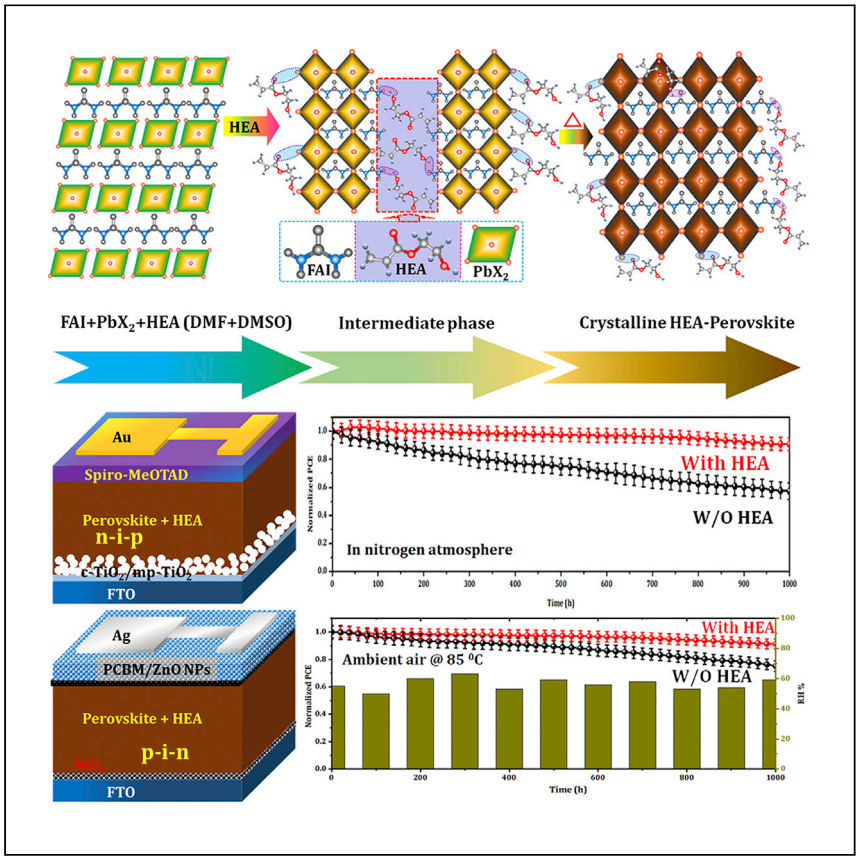

Defect passivation in halide perovskite thin films is one approach to achieve high efficiency and stability in perovskite solar cells. Here, Mali et al. adopt a 2-hydroxyethyl acrylate organic additive and use its dual functionality, producing >22% efficiency with >85% retention over 1,000 h.

Sawanta S. Mali, Jyoti V. Patil, Dae Woong Park, Young Hee Jung, Chang Kook Hong

sawantasolar@gmail.com (S.S.M.)
hongck@jnu.ac.kr (C.K.H.)

Highlights

Organic additive for defect and surface passivation of the triple cation halide perovskite

Optimized devices with n-i-p configurations exhibit >21% PCE

The HEA organic-additive-based devices exhibit 1,000 h photostability

Role of HEA additive in stability is studied by TOF-SIMS analysis

Mali et al., Cell Reports Physical Science 3, 100906
June 15, 2022
https://doi.org/10.1016/j.xcrp.2022.100906

Cell Reports
Physical Science

CellPress
OPEN ACCESS

Article

Intrinsic and extrinsic stability of triple-cation perovskite solar cells through synergistic influence of organic additive

Sawanta S. Mali,[1,3,*] Jyoti V. Patil,[1] Dae Woong Park,[1] Young Hee Jung,[2] and Chang Kook Hong[1,*]

SUMMARY

Surface- or bulk-passivation using organic additives plays a critical role in improving the performance and stability of hybrid perovskite solar cells (HPSCs). Here, we report 2-hydroxyethyl acrylate (HEA) as an additive to reduce crystallization and passivate defects. Because of the dual functionality of the HEA additive, the optimized HPSCs yield 22.05% and 21.46% power conversion efficiency (PCE), respectively, for mesostructured negative-intrinsic-positive (*n-i-p*)- and planar positive-intrinsic-negative (*p-i-n*)-type device configurations, which is much higher than control devices. Large devices with 1 cm^2 active area also produce a promising 20.03% PCE, which is comparable to the current efficiency. Time-of-flight secondary ion mass spectroscopy (TOF-SIMS) measurement analysis indicates the HEA settles not only in grain boundaries but also within the perovskite grain, which facilitates passivation and suppresses halogen-ion migration. Importantly, photostability analysis reveals negligible efficiency loss over 1,000 h under continuous 1 sun illumination under different environmental conditions.

INTRODUCTION

Nowadays, hybrid perovskite solar cells (HPSCs) have attracted tremendous interest in low-cost, next-generation solar cells due to a prompt progress in device efficiency from 3.8% in 2009 to 25.7% in approximately the last decade.[1–6] Perovskites are represented by the general chemical formula ABX_3, where A is a monovalent organic/inorganic cation, typically MA^+, FA^+, or EA^+ (herein, MA stands for methylammonium cation, FA stands for formamidinium cation, and EA stand for ethylammonium cations).[7–9] Furthermore, alternative organic cations such as cesium (Cs^+) or Rb^+ for all-inorganic PSCs (IPSCs) have been used.[10,11] The B is a divalent metal cation such as Pb^{2+}, Sn^{2+}, and Ge^{2+},[12,13] and X is a halide anion such as Cl^-, Br^-, I^-, and their mixtures.[14,15] Unique compositions developed using triple and quadruple cation-incorporated ABX_3 perovskites have proven to be a powerful approach toward tuning both the efficiency and stability of devices made from these materials.[16,17]

Tremendous efforts have been made toward the use of perovskites based on multiple cations. These cations facilities dramatically improved the efficiency by controlling morphology and interfaces. However, organic cation components still need to be stabilized against moisture- and thermal-induced stresses. In addition, large-grain boundaries and non-uniform film surface areas hinder their moisture stability. Therefore, developing different approaches that are able to tune film morphology with reduced grain boundaries will be important to improving long-term stability. The use of additives during synthesis of perovskite thin films can facilitate grain

[1]Polymer Energy Materials Laboratory, School of Chemical Engineering, Chonnam National University, Gwangju 61186, South Korea

[2]Advanced Chemical Materials R&D Center, Korea Testing & Research Institute, Gwangyang 57765, South Korea

[3]Lead contact

*Correspondence: sawantasolar@gmail.com (S.S.M.), hongck@jnu.ac.kr (C.K.H.)

https://doi.org/10.1016/j.xcrp.2022.100906

boundary and surface passivation, as well as enhanced crystallinity. Based on above aspects, Bai et al. reported >1,800 h at 70°C–75°C long-term operational stability using 0.3 mol % 1-butyl-3-methylimidazolium tetrafluoroborate ($BMIMBF_4$) ionic liquid additives under continuous simulated AM1.5 illuminations.[18] Yang et al. demonstrated 1,200 h stability at 65°C using a thin layer of lead oxysalts.[19] Zheng at al. used different chain lengths of alkylamine ligands (AALs) to modify the grains as well as the interface passivator, which produces a 22.3% power conversion efficiency (PCE) with a stable performance of over 1,000 h stability.[20] Similarly, Na et al. used 2-hydroxyethyl acrylate (HEA) in perovskite precursors as well as in anti-solvents in order to retard the crystallization process of perovskite and to take advantage of the dual functionality of HEA additives to increase the grain quality and defect passivation with 20.4% PCE.[21,22]

Where cross-linking molecular chains are concerned, Yang et al. used tetra-ethyl ammonium (TEA) as a hydrophobic layer to the perovskite surface, which enabled highly efficient and moisture-resistant perovskite thin films. The fabricated HPSCs using TEA passivation yielded a more than 15% PCE with >30 days stability under 90% relative humidity (RH).[23] Similarly, Li et al. applied alkylcarboxylic acid ω-ammonium chlorides (ABPA) to cross-link the perovskite layer and demonstrated enhanced moisture tolerance as well as thermal stability.[24] These cross-linking additives either cross-link adjacent grains or act as nucleation sites to grow the perovskite crystals.[25,26] Therefore, grain-boundary passivation significantly affects device performance as well as stability.

In order to achieve the chemical modification or grain-boundary passivation between two adjacent grains, it is necessary to occupy the cuboctahedral site with external additives. However, the external additives should not enter in the perovskite lattice in order to maintain its original photoactive properties. This approach synergistically acts as an increased grain-boundary passivation, resulting in improved device performance and stability and improved film adhesion through inter-grain bridges, and offers limited nucleation sites to improve the film morphology and suppress and/or passivate defect states.[27,28] A number of organic passivators have been used to tune the film quality as well as the stability of HPSCs, as is overviewed in Table S1.

Noel et al. adopted a thiophene and pyridine molecule passivation approach to reduce the nonradiative decay and to make a making stable perovskite layer via Pb^{2+} coordination. The sulfur (S) and nitrogen (N) atoms, respectively, from thiophene and pyridine molecules provide a lone pair. This lone pair facilitates Pb-ion coordination through electrostatic attraction between the positive charge on the metal and the lone pair.[29] These S and N functional groups facilitate Lewis bases and produce a Lewis adduct that enables crystal surface passivation.[30,31] Wen et al.[32] and Zeng et al.[33] independently proved that the Lewis-base additives, which are derived from 3-hexylthiophene and poly(3-hexylthiophene-2,5-diyl) (P3HT), were able to form bonds with uncoordinated Pb^{2+} ions, which facilitates a passivation effect. Hou et al. used oleylammonium polysulfides (OPs) as a surface atomic modulator and demonstrated 14 days of stability under 40% $\pm$ 10% RH.[34] Based on the aforementioned discussion, it is clear that the additives with functional groups with C=O, S=O, or P=O tails can effectively control not only the perovskite crystallization process but can also contribute in defect bulk and surface passivation.[35–39] In addition, hydroxyl groups (−OH) and carboxyl groups (−COOH) can efficiently act as Lewis bases and passivate uncoordinated Pb^{2+} defects by forming Pb–O bonds with the Pb ions.[40,41]

In this investigation, we report the dual functionality of the HEA additive in triple-cation $Cs_{0.175}FA_{0.750}MA_{0.075}Pb(I_{0.880}Br_{0.120})_3$ (referred to as CsFAMA) perovskite for controlling their crystallization and improved morphology, charge transport, and defect passivation and hindering the transport channels for ion migration. The HEA containing the O–H as well as C=O functional groups synergistically has an effect on device performance and stability. The grain-boundary and surface passivation were done by providing a lone pair through the C=O and –OH functional groups of the HEA additive. We systematically investigated the influence of the HEA and each functional group C=O or O–H on device performances and perovskite-film formation. The role of HEA in the CsFAMA perovskite crystallization process is investigated by Fourier transform infrared (FT-IR), X-ray photoelectron spectroscopy (XPS), and nuclear magnetic resonance (NMR) measurement techniques. Our results show that the HEA additive is not included in the crystal interior during the crystallization process. However, it plays a key role in improving the grain growth of the perovskite thin films. An optimized concentration of HEA produces 22.08% and 21.46% PCE, respectively, for negative-intrinsic-positive (*n-i-p*) and positive-intrinsic-negative (*p-i-n*) device configurations, which are much higher than control devices with no additives. Interestingly, both types of devices exhibited >1,000 h photostability under different environmental conditions.

RESULTS AND DISCUSSION

Growth mechanism

For simplicity, we discussed growth mechanisms based on only FAI (herein FA^+, MA^+, Cs^+) and PbX_2 (PbI_2 and $PbBr_2$) precursors. Initially FAI and PbX_2 precursors were dissolved in dimethylformamide (DMF)/dimethyl sulfoxide (DMSO) (4:1 v/v) solvent. This perovskite precursor solution is deposited on top of the fluorine-doped tin oxide (FTO)/c-TiO_2/mp-TiO_2 layer using the anti-solvent method (Figure 1A). Here, PbX_2 acts as a Lewis acid that combines with the DMF and DMSO Lewis bases. Simultaneously, FA^+ also interacts with DMF or DMSO due to electrostatic charge, which results in a decrease in the coordination of PbX_2. During crystallization of the perovskite thin film via the conventional method, the FAI and PbX_2 interaction is high; therefore, they could react quickly in the anti-solvent process, resulting in the formation of regular perovskite grains.[36,42] In contrast, when we applied the HEA additive, the O–H group of HEA forms a hydrogen bond with FA^+ instead of DMF or DMSO, and therefore, the coordination bond of PbX_2 will be improved due to excess DMF and DMSO molecules. After the anti-solvent treatment, the precursor solution converted into the intermediate CsI-FAI-DMSO-DMF-HEA-PbX_2 complex. As discussed previously, the advantage of the anti-solvent method is that the perovskite grains start to grow from nuclei centers to form grains. At this stage, the hydrogen bonds of the FA^+ cations and HEA are broken. The presence of the HEA additive partially hinders the reaction between FAI and PbX_2 and results in the retardation of the crystallization process, which enables increases in the grain size.[42] Meanwhile, the HEA settles at the perovskite grain boundary along with DMF and DMSO residues. During the annealing process at 100°C, the DMF and DMSO residues evaporated; however, HEA will settle on the perovskite grain boundary as well as on the film surface. It is also noted that the HEA additive is deposited to depths inside the perovskite film before complete crystallization of the perovskite phase.[25,41] Furthermore, it is also expected that the hydroxyl groups (−OH) from HEA enable the formation of a hydrogen bond with Pb^{2+}, halides, and FA^+ cations.[43] Besides, the -OH group acts as a Lewis base and passivates uncoordinated Pb^{2+} through Pb–O bonds with the Pb ions' bond formation.[40,44] It is also possible that, even after the annealing process, a few HEA molecules that bridge between two

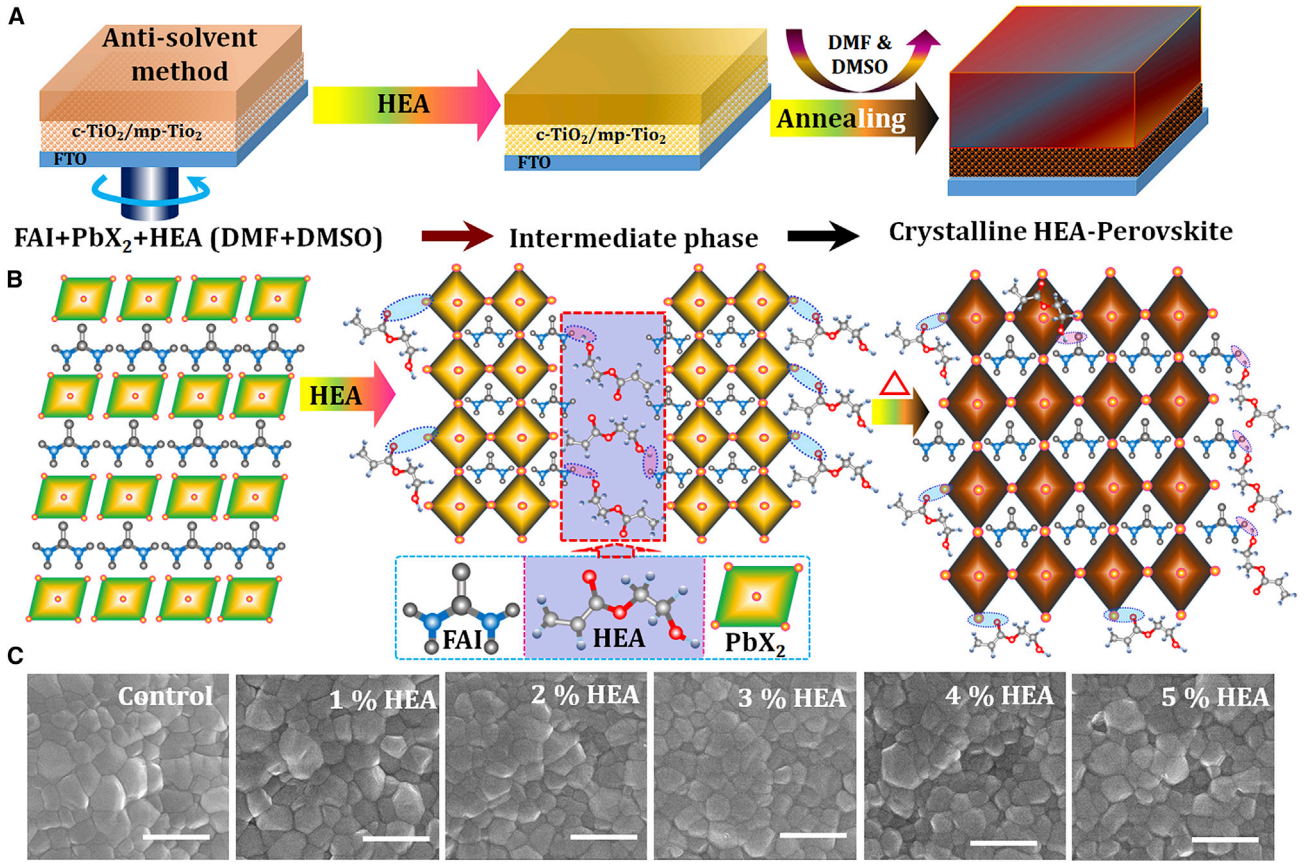

Figure 1. Methodology and growth mechanism

(A and B) Schematic representation (A) and growth mechanism (B) of perovskite thin-film formation through HEA additive.

(C) Surface morphology of respective perovskite thin films deposited on FTO/c-TiO_2/mp-TiO_2 ETLs.

Scale bar, 500 nm. All SEM images were recorded using beam intensity 15 kV at 30 k magnification.

adjacent grain boundaries and surface, which cross-links two adjacent grains, passivate the grain boundary defects.

The influence of C=O and C-OH species from HEA additives in the crystallization process and its film formation has been systematically studied with the help of FT-IR and NMR spectroscopy. The precursor solution, along with HEA addition, was used for FT-IR measurements. The FT-IR spectra of the perovskite precursors, bare HEA, and HEA-additive-based solutions were recorded (Figure S1A). Figures S1B–S1D show magnified fingerprint regions for S=O, C-OH, and C=O bonds. The FT-IR spectrum of the HEA solution exhibited a broad peak at 3,425 cm^{-1} assigned to C–OH stretching. The broad peak at 1,720 cm^{-1} corresponds to carbonyl groups (–C=O) stretching, while –CH = CH– stretching reflected from doublet peaks at 1,637 and 1,619 cm^{-1}. Furthermore,–CH_2 stretching appears from the peak position at 1,410 cm^{-1} (Figure S2). For a bare perovskite precursor, a sharp and strong signal appears at 1,658 cm^{-1} due to C=O stretching, which arises due to DMF. The presence of S=O stretching of DMSO was revealed from the peak position at 1,017 cm^{-1}. We observed that the weak C–OH peak at 3,400 cm^{-1} in the control and HEA + CsFAMA samples arises due to atmospheric moisture. Interestingly, we observed a considerable peak shift in C–OH for the perovskite + HEA sample. However, a negligible peak shift was observed in the C=O stretching after HEA

addition. These FT-IR analyses revealed that the HEA additive interacted with the perovskite precursor due to a dominating interaction by the C–OH bond and was not affected by the C=O functional group. On the other hand, the S=O and C=O bonds facilitate coordination between DMF and DMSO toward PbX_2 species.[45] After the addition of HEA, the C–OH, S=O, and C=O peaks are shifted toward a lower wavenumber and broaden, indicating the HEA and perovskite precursor interaction. This peak shift toward a lower wavenumber is due to decreased bond strengths between C=O and S=O and the formation of an adduct.[46] Thus, we conclude that the HEA additive helps in the formation of the adduct, which improves the coordination capabilities of DMF and DMSO to Pb^{2+}. Our individual FTIR spectra of FAI, MABr, PbI_2, $PbBr_2$, and CsI with HEA show similar peak positions of C=O stretching, indicating no interaction with the C=O bond of the HEA additive (Figure S2C). In contrast, the C–OH stretching vibration shifted to 3,332 from 3,425 cm^{-1} for the FAI + HEA precursor solution (Figure S2B). The aforementioned results indicate that the FA^+ organic cation has strong interactions with the HEA additive. In contrast, inorganic cations such as PbI_2, $PbBr_2$, and CsI have no interactions with the HEA additive, which is confirmed by the unchanged characteristic peaks for C–OH and C=O functional groups (Figure S2C). From the FT-IR results, it is clear that the –OH functional group from HEA is playing a critical role through organic cation interactions (Figure S2D). This interaction toward organic cations increases the free DMF and DMSO molecules. Hence, there is improved relative binding of free DMF to Pb^{2+} or free DMSO and Pb^{2+}. Therefore, this HEA addition is not taking part in the formation of HEA-PbX_2's intermediate phase. However, it will help to coordinate bonding between DMF and Pb^{2+} and between DMSO and Pb^{2+} by strongly interacting with the organic cations.

To investigate the organic cation and HEA interaction, we obtained NMR spectroscopy measurements (Figure S3). The ^1H NMR spectra of the bare FAI and MABr powders were recorded from deuterated DMSO-d6 solvent. As expected, bare cations exhibited MA ($–NH_3^+$) and FA ($–NH_2^+$) signals at δ = 7.71 and 8.75 ppm, respectively, corresponding to characteristics of MA^+ cation–Br^- anion ($C–NH_3\cdots Br^-$) and FA^+ cation I^- anion ($C–NH_2\cdots I^-$) hydrogen bonding.[47,48] The NMR spectrum of the FAI + MABr + HEA sample indicates a positive chemical shift up to $\Delta\delta \approx 0.14$ ppm (8.89 ppm) and a weak negative chemical shift of $\Delta\delta \approx 0.12$ ppm (8.63 ppm) attributable to the N–H bonds of FAI. Therefore, the $-NH_2^+$ peak signal was poor and split into two separate signals. Similar results were observed for $-NH_3^+$ peak. This peak shift is attributed from the formation of hydrogen bonds N–H···H–O between organic cations with the HEA additive. This hydrogen bond enables the delocalization of the electron cloud of the N–H bond as well as weakening the N–H chemical bond, reducing their corresponding frequencies.[49] The broad O-H resonance peak for FAI + MABr + HEA revealed N–H···H–O bond formation between HEA and FA^+ and MA^+ cations. From our FT-IR and NMR analysis, it is clear that the –OH from HEA can form a strong hydrogen bond with FA^+ cations in precursor solution, which facilitates increased crystallinity and grain size. Furthermore, it is also observed that the -OH group from the HEA additive retards crystallization significantly, leading to improved film quality. The small remaining amount of HEA participates in passivation of the trap states, which facilitates improved device performance and stability.

Surface morphological analysis

To understand the aforementioned mechanism for the grain-size and performance enhancement, we recorded scanning electron microscopy (SEM) images of the CsFAMA thin films containing various volumes of the HEA additive. Top-view SEM

images of perovskite films deposited on a FTO/c-TiO_2/mp-TiO_2 layer with different concentrations of the HEA additive are shown in Figure 1C. From SEM analysis, it is clear that the control sample exhibited an average grain size around 185.95 nm that was non-uniformly distributed. In contrast, the 1% HEA-additive-based sample exhibited a narrow range of grain-size distribution (Figure S4). Besides, the 1% HEA added produced much larger grains, with an average size of 222.08 nm. In addition, the SEM image of the 1% HEA additive shows well-defined grains with limited distinctive grain surfaces and limited grain boundaries. These results reveal that the HEA additive could improve the film morphology. In the second case, 2% HEA reduces the average grain size (154.76 nm), which may be due to increasing amounts of heterogeneous nuclei centers. In short, the grain size and morphology of the perovskite thin film is dependent on nucleation density. Therefore, the grain size decreased because of higher (3%–5%) HEA concentrations. Therefore, this enlarged grain of the 1% HEA-based sample reduces the grain boundaries and defects, thereby improving the charge-transport properties and suppressing the charge-recombination centers.

Atomic force microscopy (AFM) images of the control and HEA-additive-based samples are very consistent with SEM images (Figure S5). The control sample exhibits an initial root mean square (RMS) surface roughness of 27.264 nm, which decreased to 18.792 nm when 1% HEA was added, indicating a smoother surface than the control sample. However, the 2% HEA sample exhibited a further increase in RMS value up to 22.455 nm, exhibiting a rougher film surface. Notably, all thin films exhibited nanometer-scale RMS roughness values due to our well-optimized anti-solvent method. This higher RMS value stems from the disorderly oriented perovskite grains with numerous grain boundaries.

Structural properties of the deposited CsFAMA perovskite thin films were studied by X-ray diffraction (XRD) measurements (Figure 2A). The intensity of the characteristic peaks was slightly enhanced for 1% HEA additives compared with control, suggesting that the HEA significantly affected the crystal-growth results in a preferred orientation, which is consistent with our SEM morphology (Figure 2A). All XRD pattern reflections match well with triple-cation CsFAMA composition.[21,50] Interestingly, we have not observed any peak shift for various HEA concentrations. This unaltered main XRD peak suggests that the HEA does not incorporate into and perturb the crystal lattice. On the other hand, we observed that the intensity of the main diffraction peaks was slightly increased, indicating enhanced crystallinity or texturing.[18] To investigate how HEA participates in the crystallization process, we analyzed the characteristic XRD peaks using full width at half maximum (FWHM) values. Figure 2B exhibits the variation in FWHM of (001) peaks from different HEA concentrations. The FWHM decreased from 0.2985 to 0.1788 Å after 1% HEA addition, which resulted in increased crystal size from 28.02 to 46.77 nm, revealing the key role of the HEA additive in crystallization and crystal growth.[21] The CsFAMA perovskite containing the 1% HEA additive showed the lowest FWHM values for the (100) peak, indicating the formation of larger crystallites according to the Scherrer formula, which facilitates high crystallinity (Figure S6). It is also noted that the (001) peak intensity of the 1% HEA-additive-based sample increased, revealing the better crystallinity. In contrast, further addition of HEA results in a decreased crystallite size up to 28.77 nm (Figure S6). This is also in good agreement with the increased grain size of the 1% HEA-based perovskite film compared with all other samples observed in SEM micrographs.

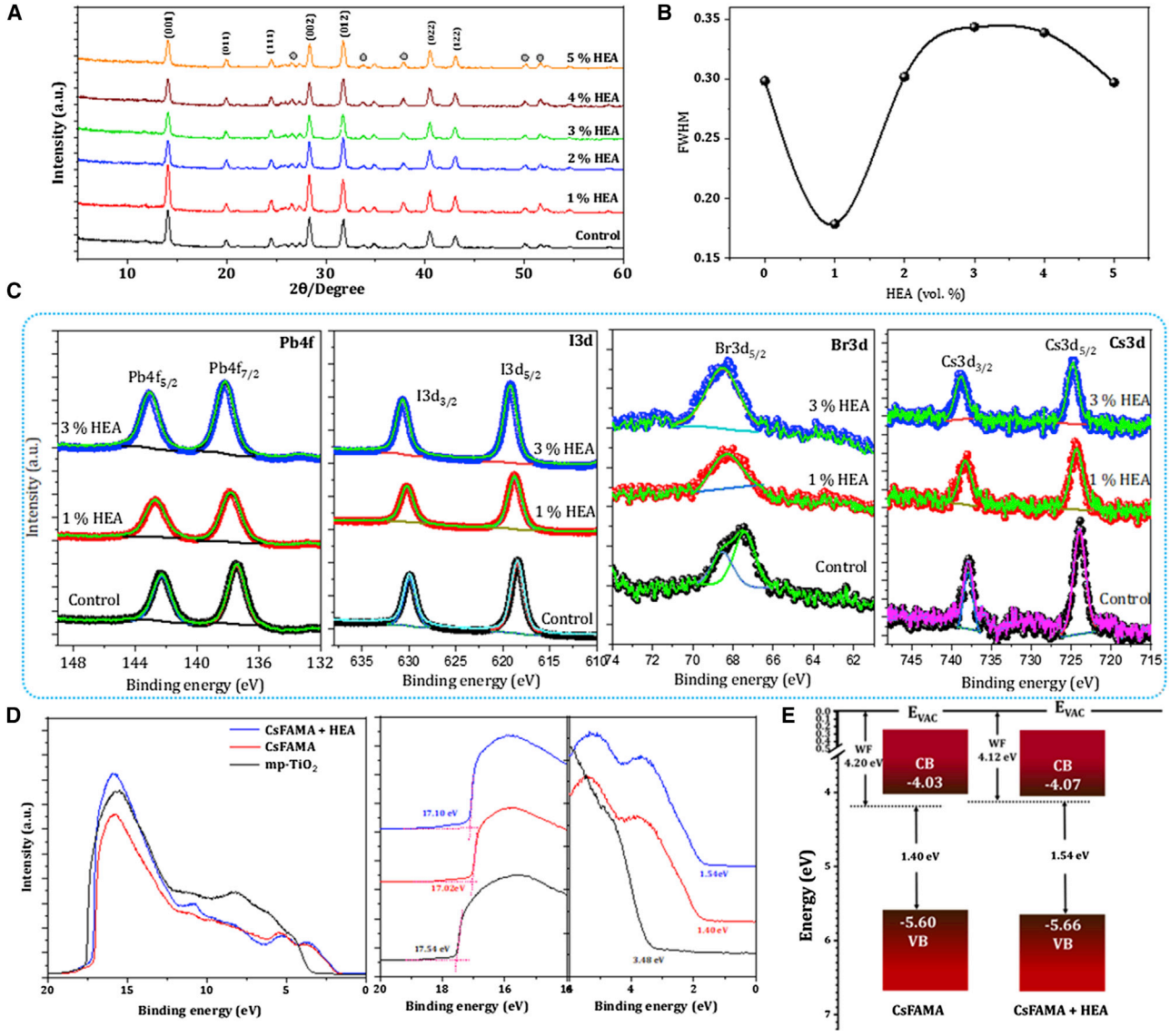

Figure 2. Structural properties of CsFAMA + x% HEA perovskite thin films

(A) XRD patterns.

(B) Circle symbol (○) represents peaks from substrate full width at half maximum (FWHM) of characteristic XRD peaks of perovskite for various HEA concentrations.

(C) X-ray photoelectron spectroscopy (XPS) spectra of Pb *4f*, I *3d*, Br *3d*, and Cs *3d* core-level peaks of perovskite films for control and 1% and 3% HEA additions.

(D) Ultraviolet photoelectron spectroscopy (UPS) spectra (using the He-I line with photon energy of 21.22 eV): magnified cutoff (E_{cutoff}) energy regions, and valence band region (VBM) onset regions of the bare CsFAMA film and with 1 % HEA + CsFAMA perovskite thin films with respect to the Fermi energy (E_F). E_{VBM} onsets were determined from semi-log plots (Figure S10A). Optical band gap was calculated from Tauc plots (Figures S10B and S10 C).

(E) Energy-level scheme for the pristine CsFAMA and 1% HEA + CsFAMA-based thin films on the parameters derived from UPS spectra.

XPS

In order to check changes in the chemical interaction and composition in the presence of the HEA additive, we obtained the XPS spectra of the control and 1% and 3% HEA-additive-based perovskite thin films (Figures 2C and S7). The four main peaks of Pb *4f*, I *3d*, Br *3d*, and Cs *3d* core levels are shown in Figure 2C. The Pb $4f_{7/2}$ core-level spectra at 137.4 eV in the control film could be ascribed to the

Pb-I binding energy of triple-cation CsFAMAPbI$_3$ perovskite composition. When the perovskite films were processed using HEA additive, the Pb *4f*, I *3d*, Br *3d*, and Cs *3d* characteristic peaks shifted to a higher binding energy. For example, the Pb $4f_{7/2}$ core-level peaks of 1% and 3% HEA-based film were shifted to higher binding energies of 137.78 and 138.16 eV, respectively (Table S2), which suggests that electronic passivation occurs after HEA is added onto the perovskite film. Similarly, I $3d_{5/2}$ core-level peaks moved to higher energies from 618.43 to 618.72 and 619.19 eV, respectively, for 1% and 3% HEA additions. In the case of the Br 3d core level, we found shifts toward higher values compared with those in the pure CsFAMA crystal, suggesting that the chemical state of the $[PbBr_6]^{4-}$ octahedral is altered and that the interactions between Pb-Br and Cs-Br are enhanced after HEA addition.[51,52] This HEA addition can affect the size of the $[BX_6]^{4-}$ octahedral, and hence, multiplicity of the Br *3d* signal is reduced, which changes the electron cloud density. This indicates that there is an interaction between HEA and perovskite.[24,53,54] In the case of Cs $3d_{5/2}$ core levels, we observed peak positions towards higher binding energies (BEs) that appeared at 723.96, 724.31, and 724.79 eV, respectively, for control and 1% and 3% HEA. From the aforementioned discussion, it is clear that there are multiple interactions, such as Pb^{2+} with C=O and FA^+ and MA^+, Pb^{2+}, I^-, and Br^- with O–H sites from HEA additive. The presence of HEA molecules was also traced from the O1s peak analysis. In addition, N *1s* and O *1s* peaks shifted to higher BEs, which revealed a chemical interaction between the perovskite and HEA (Figure S8). Any chemical composition changes of oxygen atomic percentage in control and HEA-based devices could be related to the presence of HEA additives. Therefore, we analyzed the atomic percentage of O *1s* of control and 1% and 3% HEA-additive-based CsFAMA films. Our XPS atomic-percentage results revealed that the O *1s* atomic percentage increased from 6.78% and 7.89% to 8.74% respectively for control and 1% and 3% HEA-additive-based CsFAMA thin films (Table S3). On the other hand, the atomic percentages of other elements were found to be relatively identical. Besides, the oxygen/iodine (O:I) ratio increased from 0.1536 (control) and 0.1781 (1% HEA) to 0.1988 (3% HEA) (Figure S9). These results revealed that the relative oxygen content is increased even though the obvious bonding of oxygen in the atmosphere is considered. These results clearly indicate that the HEA is present on the surface of the perovskite film.[21,55]

Ultraviolet photoelectron spectroscopy

The electronic structures of the perovskite thin film before and after HEA addition were analyzed by ultraviolet photoelectron spectroscopy (UPS) (Figures 2D and S10). The work function (WF) and valence-band maximum (VBM) were calculated from the BE cutoff (E_{cutoff}) and the BE onset (E_{onset}) (Figure 2D). The corresponding (E_{cutoff}, WFs) values of each layer were estimated to be (17.54 eV, 3.68 eV), (17.02 eV, 4.2 eV), and (17.10 eV, 4.12 eV), respectively, for mp-TiO_2, control, and 1% HEA samples. The VBM energy level can be calculated from the equation $E_{VBM} = h\nu - E_{cutoff} + \Delta E_g$, where hν = 21.22 eV for He-I. From UPS, E_{onset} values were estimated to be 3.68, 4.2, and 4.12 eV and the E_{VBM} values were estimated to be 7.16, 5.6, and 5.64 eV, respectively, for mp-TiO_2, control, and the 1% HEA sample (Table S4). The VBMs were located 1.4 and 1.54 eV below the Fermi level (E_F) for CsFAMA and the 1% HEA-based CsFAMA films, respectively. Figure 2E shows calculated energy-level diagrams based on UPS and optical absorption measurements. Interestingly, the VBMs and conduction-band maximum (CBM) positions after HEA addition were not changed drastically. In contrast, the WF shifts by 80 meV towards the vacuum level (E_{VAC}), and the E_F shifts by 140 meV toward the CBM, indicating that the HEA addition facilitates more *n*-type charge carrier. This more *n*-type behavior stems from the HEA molecule by donating electron density to the Pb from the -OH lone

pair, leading to the formation of a coordinate bond. This more *n*-type charge carrier contains a higher number of charge traps, which dominate trap species, leading to decreased trap-assisted recombination and crystal passivation. Therefore, perovskite films containing higher *n*-type behavior enable better charge extraction toward mp-TiO_2 electron transport layers (ETLs).[56–59]

We conclude that the C=O and –OH functional groups from the HEA additive play key roles in the coordination of Pb^{2+} while excess HEA molecules settle on the perovskite grains, which terminates the grain growth and constrains the grain-tilt growth, leading to (100)-oriented grain growth. This controlled grain growth facilitates lower defect density.[60] As our XRD and XPS analyses revealed, HEA does not contribute in the perovskite lattice. Considering the HEA additive distribution within perovskite films and grain-boundary passivation, the excess HEA additive also settled at grain boundaries, which was confirmed from point energy-dispersive spectroscopy (EDS) mapping (Figures S11–S13). An increase in the oxygen concentration resulted in its aggregation at the boundaries and at the film surface, resulting in improved stability. Therefore, the HEA additive not only passivates the grain boundaries but also improves the stability.

Device architecture and photovoltaic performance

Generally, mesostructured *n-i-p* HPSCs produce better photovoltaic parameters and reproducibility. Therefore, in order to evaluate the role of HEA on solar cell performance, initially we fabricated normal *n-i-p* mesostructured device architectures of the HPSCs. The additive-doped spiro-MeOTAD hole transport material (HTM) has been spin-coated onto the perovskite thin films followed by 80 nm gold deposition, and its schematic device configuration is shown in Figure 3A. The cross-sectional images of the control and 1% HEA-additive-containing CsFAMA perovskite-based devices are shown in Figures 3B and 3C. Nearly 453 nm thick, a uniform pinhole-free absorber layer was formed on up to a ~180 nm mp-TiO_2 layer for the control device. Interestingly, the 1% HEA-based device exhibited similar film thickness. The average thicknesses of the perovskite films for control and 1% HEA were ~453 and ~476 nm, respectively. However, we observed that the perovskite capping layer of the HEA-based device had well-defined large grains in the vertical direction. Generally, different experimental conditions such as precursor solubility, spin-coating speed, and viscosity of the precursor solution and additives strongly affect the film quality during synthesis.[61] Here, the HEA additive played a key role in controlling the crystallization and resulted in highly crystalline and well-defined controlled grain growth. Therefore, the 1% HEA-based sample leads to the formation of a highly uniform perovskite thin film with well-defined smooth-grain boundaries.

The UV visible (UV-vis) absorption spectra of the respective perovskite thin films with different HEA concentrations are shown in Figure 3D. We observed that samples with and without HEA added exhibited identical band edges, revealing that HEA does not affect the composition or is not inserted into the perovskite lattice. However, it is noted that the 1% HEA-based sample exhibited slightly higher absorption than the other sample owing to the increased grain size, which facilitates improved light scattering within perovskite grains.[42] Although we observed negligible improvements in film absorption, the steady-state photoluminescence (PL) intensity was enhanced, which indicates reduced defects in the 1% HEA-based film compared with other HEA concentrations (Figure S14). We also investigated the role of the HEA additive on the electron lifetime by using time-resolved PL (TRPL) analysis (Figures 3E and S15), and the fitted parameters are tabulated in Table S5 (Note S1).[62,63] The TRPL lifetime of the control sample was extended from 6.72 to

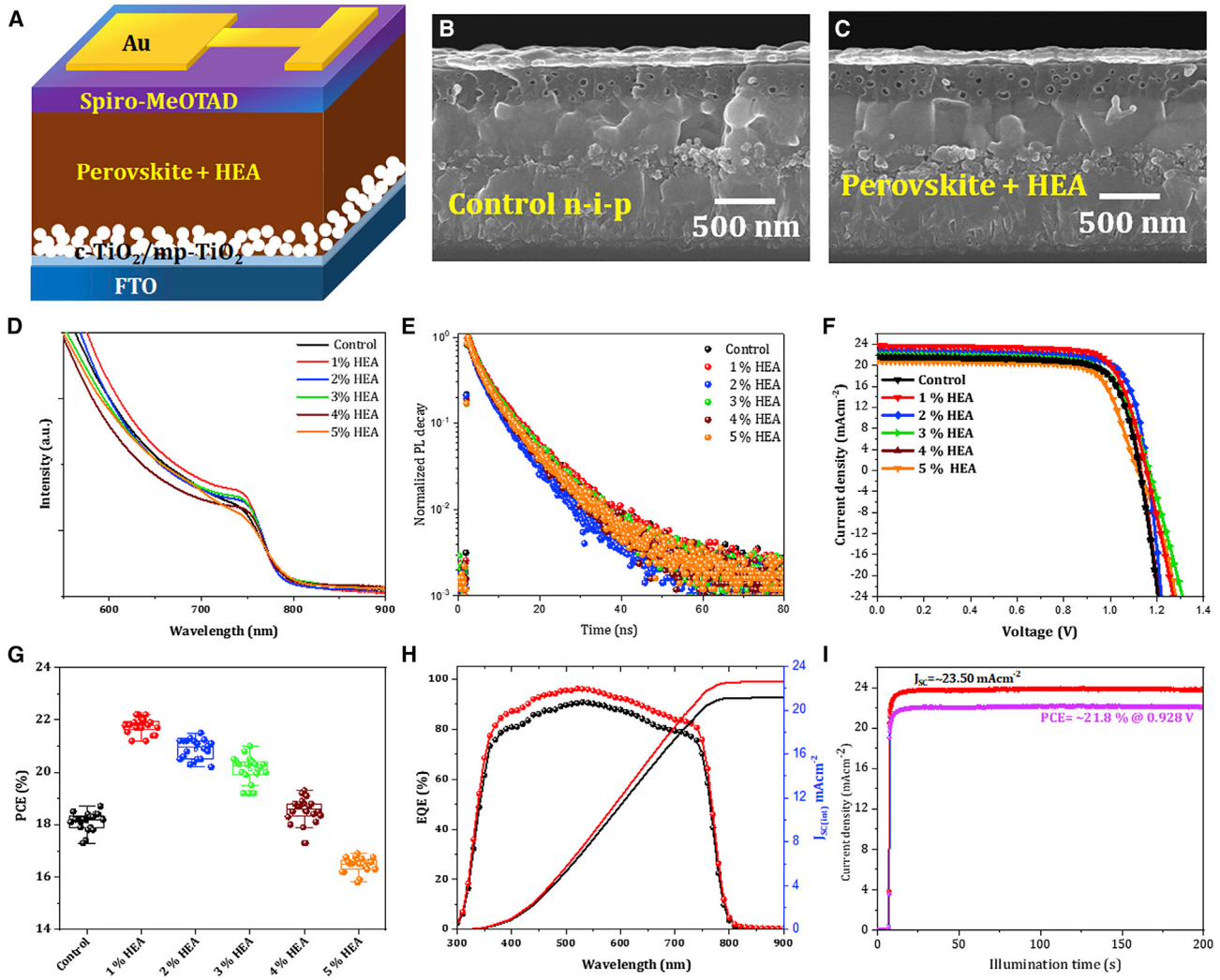

Figure 3. Normal *n-i-p* device configuration and photovoltaic properties

(A) Schematic device configuration of PSC.

(B) Cross-sectional SEM image of CsFAMA-based PSC device without HEA additive.

(C) Cross-sectional SEM image of CsFAMA-based PSC device containing 1 % HEA additive.

(D) UV-vis absorption spectra of perovskite thin films with various concentration of HEA additive.

(E) TRPL spectra of perovskite thin film deposited on FTO/c-TiO_2/mp-TiO_2 substrates.

(F) Current-voltage (J-V) curves measured under standard AM1.5 solar radiation.

(G) Device reproducibility for at least 20 identical devices. Error bar, ±5%.

(H) EQE spectra of control and 1% HEA-based devices.

(I) Steady-state current density monitored at maximum power point bias and respective stabilized PCE of PSCs of the 1% HEA-based champion device.

7.05 ns after 1% HEA addition, which revealed reduced grain boundaries and recombination centers within the perovskite thin films. The TRPL analysis revealed that the CsFAMA thin film containing 1% HEA exhibited a longer carrier lifetime than the control (0% HEA, τ = 6.72 ns) and other HEA concentrations. This longer carrier lifetime in the 1% HEA-processed perovskite sample indicates that the carrier non-radiative recombination was significantly reduced by elimination of defects and a light-trap annihilation mechanism.[58,64] Although, we have observed a small lifetime decay, which is due to FTO/c-TiO_2/mp-TiO_2 ETLs. Therefore, in order to check for the exact lifetime of our control and 1% HEA-based samples, we deposited perovskite film on FTO/Al_2O_3 substrates, which isolate the perovskite-absorbing layer properly. From

Table 1. Photovoltaic performance of regular TiO_2 ETL-based *n-i-p*-type HEA-based perovskite solar cells

Device	V_{OC} (V)	J_{SC} (mA cm^{-2})	FF	PCE (%)
Control	1.124	21.88	0.75	18.45
1% HEA	1.156	23.85	0.80	22.05
2% HEA	1.157	22.75	0.76	20.01
3% HEA	1.165	22.34	0.74	19.25
4% HEA	1.128	22.05	0.72	17.91
5% HEA	1.115	20.86	0.70	16.28

TRPL analysis, it is clear that the 1% HEA CsFAMA sample exhibited a 54 ns lifetime, which is much higher than control samples (37 ns), indicating reduced defects in the 1% HEA-based perovskite film (Figure S16; Table S6).

Photovoltaic performance

To evaluate the influence of HEA on photovoltaic performance, the current-voltage (J-V) characteristics of the HPSC devices were measured under 1 sun illuminations. The perovskite devices fabricated from triple-cation composition exhibited an open-circuit voltage (V_{OC}) of 1.124 V, a current density (J_{SC}) of 21.88 mA cm^{-2}, and a fill factor (FF) of 0.75, yielding 18.45% PCE, which indicates that our recipe worked well (Table 1). Keeping all experiments identical, we recorded J-V characteristics for different HEA-additive concentrations (Figure 3F). For the 1% HEA addition, we observed a substantial improvement in V_{OC} and reached up to 1.154 V, yielding 21.99% PCE with a J_{SC} of 23.82 mA cm^{-2} and an FF of 0.80. With 2% HEA, we observed a further rise in V_{OC} and reached up to 1.157 V with a J_{SC} of 22.75 mA cm^{-2} and an FF of 0.76, yielding 20.01% PCE. Interestingly, the V_{OC} reached up to 1.165 V for the 3% HEA addition; however, the J_{SC} slightly decreased to 22.34 mA cm^{-2} and the FF lowered to 0.74, yielding 19.25% PCE. In other increments of HEA concentration, we observed decrement in device parameters and produced 17.91% and 16.28% PCE, respectively, for 4% and 5% HEA-additive-based perovskite devices. These results suggest that the 1% HEA additive leads to a significantly enhanced device performance due to increased grain size and crystallinity or texturing (Figure 2A). Fine-tuning of the HEA-additive concentration was done carefully; however, we believe that 1% HEA devices exhibited excellent efficiency, (Figure S17 and Table S7). Higher HEA concentrations lead to smaller grains, resulting in lower J_{SC}s and FFs compared with 1% HEA, which results in a lower PCE. In short, higher crystallinity produces higher J_{SC}s, which was consistent with our XRD analysis. Therefore, it is concluded that this improved photovoltaic performance stems from synergistic effects of improved transport and extraction of the photogenerated charge carriers due to the HEA additives. In addition, enhanced light absorption from larger grains also contributes to this improved photovoltaics performance.

To check the reproducibility of our results, we fabricated and characterized at least 20 independent devices based on various HEA concentrations. Figure 3G shows that the statistical distribution of the PCEs revealed high repeatability of the device performance. This improved device performance mainly stems from enhanced J_{SC}s and V_{OC}s of the devices (Figure S18). The control device exhibited an average 18.2% PCE, while 1% HEA-based devices exhibited an average 21.9% PCE with high reproducibility. The external quantum efficiency (EQE) of the champion devices were measured in order to validate the J_{SC} values obtained from J-V curves (Figure 3H). As expected, our control device exhibited an ~90% EQE value, which was improved to more than 95% for the 1% HEA-based device. The calculated integrated current-density (J_{int}) of the respective perovskite device exhibited J_{int} = 21.18 and 22.82 mA cm^{-2}, which validates well with

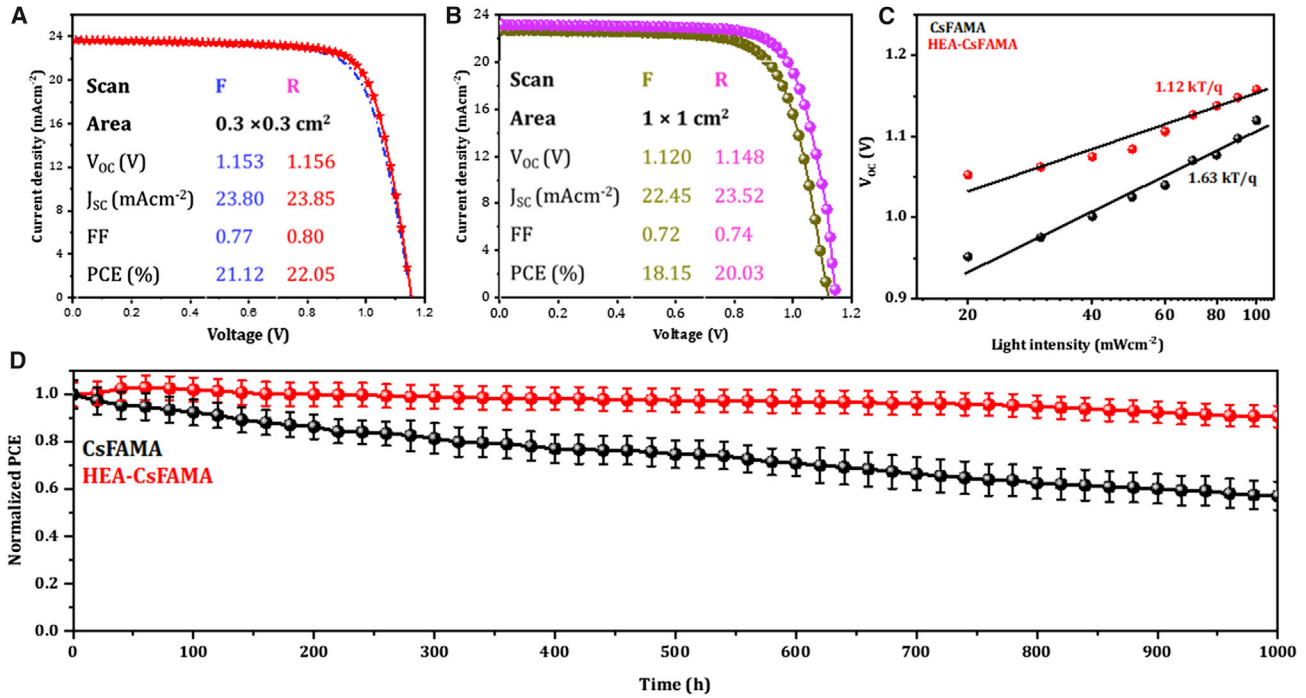

Figure 4. Hysteresis analysis and device stability of *n-i-p* devices

(A and B) Hysteresis of small-area device (A) and large-area device (B) performance of the champion device.

(C) The dependence of V_{OC} on light intensity for champion devices containing 0% and 1% HEA.

(D) Photostability recorded under 100 mW cm^{-2} white LED continuous illumination in N_2-filled glowbox at 45°C thermal stress. Error bar, ±5%.

photocurrent-density values obtained from the J-V curves. This improved photovoltaic performance of the HPSCs with 1% HEA additives stems from the synergistic effect of improved extraction and transport of photogenerated charge carriers from the high-quality perovskite grains with HEA-bulk-surface passivation and better light absorption.

To gain in-depth analysis for stability, we monitored the stabilized power output (SPO) by measuring the actual J_{SC} at a maximum power point tracking (MPPT) bias voltage of 0.928 V over 200 s (Figure 3I). Once illuminations turned on, the device attended its maximum current within 10 s to produce a stabilized current of 23.50 mA cm^{-2}. The stabilized current yielded an SPO at 21.8% with an SPO-to-PCE ratio of 0.988, which revealed that our HEA-based HPSC device had a limited trap density that reduces the trap-assisted recombination.[65–68] Considering the charge accumulation from inefficient charge transfer at the grain boundaries and interfaces,[69] we analyzed the J-V hysteresis of the control and champion 1% HEA-based devices. Hysteresis analysis revealed that our control device exhibited significant hysteresis (Figure S19). This anomalous hysteresis stemmed from ion migration to the perovskite-HTM film interface and grain boundaries, which consequently increase the hysteresis. The champion device showed negligible hysteresis with 21.12% and 22.05% PCE, respectively, in forward and reverse scans, indicating that the HEA additive does not give rise to a charge accumulation (Figure 4A). These results are consistent with our TRPL lifetime measurements. Therefore, the 1% HEA-additive-based thin film facilitates increased charge-carrier lifetime, indicating trap passivation induced by HEA in the perovskite film.

Large-area fabrication

In order to check feasibility toward large areas, we fabricated a 1-by-1 cm active-area device using 1% HEA additive. For this, a large-area device (1 by 1 cm active area) was fabricated onto a 2.1 by 2.1 cm FTO-coated substrate. The active area was defined by depositing a 1-by-1 cm square-shaped gold contact. The large-area device exhibited a PCE of 18.15% with a V_{OC} of 1.120 V, a J_{SC} of 22.45 mA cm^{-2}, and an FF of 0.72 under the forward-scan condition. On the other hand, the reverse scan exhibited a V_{OC} of 1.148 V, a J_{SC} of 23.52 mA cm^{-2}, and an FF of 0.74, yielding 20.03% PCE, indicating that the large area crosses 20% PCE with negligible hysteresis (Figure 4B). For charge transport measurements, we recorded the V_{OC} versus the illumination intensity for the control and 1% HEA-additive perovskite devices (Figure 4C). The slope of the fitted data yields values of the ideality factor (η), which was determined by $V_{OC} = nkT\ln(I)/q + A$, where k, T, and q are the Boltzmann constant, the temperature in kelvins, and the elementary charge, respectively. The A is constant according to the Shockley-Read-Hall (SRH) recombination mechanism.[70–72] The above equation can be simplified for η as $\eta = Slope \times \frac{q}{kT}$. Our control device gives an η value as high as 1.63 for the control device, which decreases to 1.12 for HEA-based devices, indicating the suppression of charge recombination. The obtained values of η indicate the dominating trap-assisted SRH recombination. These results indicate that the synergistic effect of HEA-additive surface passivation helps to reduce the recombination of charge carriers, and it is also consistent with our illumination-intensity-dependent V_{OC} variation.

Next, we investigated the defect density in the HPSC devices based on different HEA-additive concentrations with the help of space-charge-limited current (SCLC) measurements. The current-voltage (I-V) characteristics of the single-carrier devices that have FTO/perovskite + HEA/Au device architectures were used, and I-V curves were recorded in dark (Figure S20; Note S2). The defect densities (n_t) were calculated by recording trap-filled limit voltage (V_{TFL}) values. Here, we used ε = 28.8 for CsFAMA composition.[73–77] As shown in Figure S20, we calculated the V_{TFL} values for control and 1% HEA-based CsFAMA compositions as 0.775 and 0.569 V, respectively. From the above logarithmic I-V analysis, the reduced calculated trap densities (n_t) from 1.201 × 10^{16} to 0.799 × 10^{16} cm^{-3} revealed the improved charge-carrier ability in HEA-based CsFAMA perovskite thin films through improved grain quality and defect passivation, leading to improved device performance.

It is well known that although HPSCs have displayed excellent efficiency, their instability against moisture, light, and thermal stress remains a challenge in their further development. Furthermore, spiro-MeOTAD-based devices are unstable in ambient condition. Therefore, the device stability of the *n-i-p* HPSCs was conducted in an N_2-filled glove box. However, we maintained 45°C thermal stress, and photostability was monitored under AM1.5G white LED illumination without encapsulated HPSC devices. The long-term photostability at room temperature showed ~70% retention of its initial efficiency over 1,000 h. On the other hand, the 1% HEA-based HPSC device retained >90% of its initial efficiency over 1,000 h, indicating excellent photostability. This improved photostability of the HEA-based device was attributed to an increase in grain size and reduced defect sites, grain-boundary passivation, and surface passivation by the HEA additive. On the other hand, poor stability without HEA may have originated from irregular film quality and grain boundaries, surface defects, and severe ion migration.

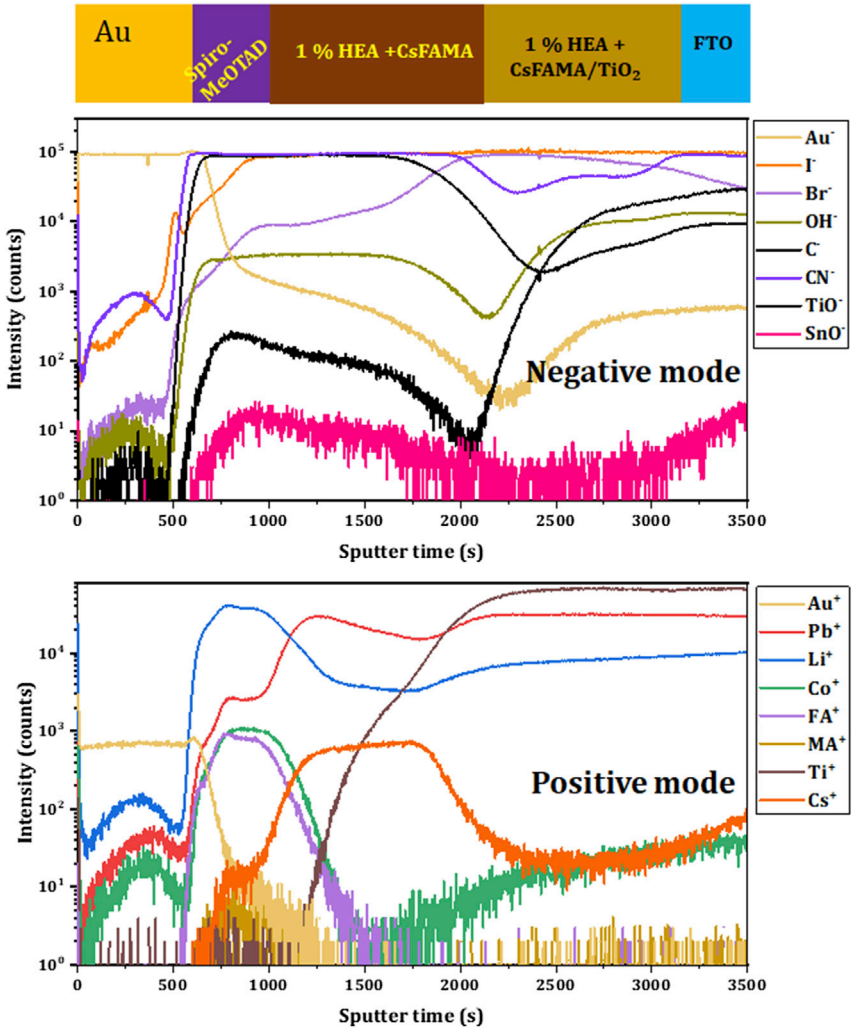

Figure 5. Depth-profile analysis

TOF-SIMS elemental depth profiles of 1% HEA + CsFAMA-based device having FTO/c-TiO_2/mp-TiO_2/perovskite/Spiro-MeOTAD/Au configuration in negative and positive modes.

Intrinsic and extrinsic stability analysis

To determine the role of the HEA additive in ion migration of the perovskite thin films, we conducted time-of-flight secondary ion mass spectroscopy (TOF-SIMS). This technique was helpful to analyze the spatial distribution of elements and halide-ion migration (Figure S21). We monitored the Au signal in the perovskite layer and the perovskite signals in the charge-transport layers, i.e., spiro-MeOTAD and TiO_2 layers of the control and HEA-based devices (Figures 5, S21, and S22). Our TOF-SIMS profile data revealed that the control sample exhibited serious Au diffusion throughout the device.[78] Perovskite halide ion migration in the spiro-MeOTAD layer as well as the TiO_2 layer was observed, which indicates that the grain boundaries allowed ion migration through grain-boundary channels. In contrast, we observed limited halide-ion migration and element diffusion in the HEA-based devices (Figure 5). This limited ion migration and diffusion of elements stems from the HEA additive, which hinders the transport channel (boundary) for ion migration.[79] Furthermore, the HEA-additive-based perovskite thin film, having an increased grain size, reduced grain boundaries, and greater passivation from the

HEA additive, hinders the transport channel (boundary) for ion migration at the perovskite spiro-MeOTAD interface, which accounts for the reduced hysteresis. For this, we monitored the I^- profile intensity of the control and 1% and 3% HEA-additive-based perovskite thin films in the Au/HTM/Perovskite region (Figure S23). Interestingly, we found that the I^- intensity decreased with respect to HEA concentration. This decreased I^- intensity in the HEA-based Au/spiro-MeOTAD/perovskite interface region stemmed from improved film quality and surface passivation, which can suppress halide-ion diffusion and mobile ion migration.[80] This could be the main reason for this reduced hysteresis in HEA-additive-based devices. It is also noted that we found some halide migration in the spiro-MeOTAD layer due to the interaction with spiro cations.[81] Therefore, we believe that the HEA-additive-based CsFAMA film not only reduces intrinsic degradation though reduced ion migration and metal diffusion but also improves device stability and performance.

Tracing HEA within the perovskite films

Next, we recorded a TOF-SIMS analysis of CsFAMA thin films with 1% and 3% HEA additives to trace the existence of the HEA additive. We monitored the O^- depth profile from surface to bottom of the perovskite films with 0% and 1% HEA concentrations (Figure S24). From TOF-SIMS depth profiles, we observed that the HEA-based CsFAMA sample exhibited a gradual decrement in the O^- signal, whereas the sample without HEA exhibited a rapid decrement up to 1,100 s sputtering time, which indicates that the HEA is distributed at the perovskite grain boundaries as well as being successfully incorporated into the perovskite grains. It is reported that the −OH and C=O functional groups from the HEA additive trigger the formation of PbI_2($PbBr_2$)-additive intermediate phases or an organic cation (FAI/MABr)-additive complex. These intermediate phases and the additive complex facilitate limited nuclei centers, which promote the formation of highly crystalline uniform grain growth.[21,35,39,44,54]

p-i-n planar heterojunction architecture

Although the regular (*n-i-p*) structure delivers peak efficiency, most n-i-p devices are based on additive-doped spiro-MeOTAD HTMs, which suffer from poor air-moisture stability. In contrast, dopant-free HTMs in either *n-i-p* or *p-i-n* devices have attracted great interest due to their long-term operational stability.[82–84] Due to a non-radiative recombination of photogenerated charge carriers, most of the *p-i-n*-type devices exhibit major photo-voltage loss. Therefore, if we passivate the defect and grain boundaries with the HEA additive, it is expected that the device performance of the *p-i-n*-type HPSCs will be improved. In order to check suitability toward *p-i-n* device configuration, we further fabricated perovskite devices based on NiO_x and PCBM/ZnO HTLs and ETLs, respectively. Figure 6A shows the schematic representation of the *p-i-n*-type planar-heterojunction-device architecture. For convenience, we have used only optimized device conditions such as 0% HEA and 1% HEA for further study. Devices were completed by depositing PCBM/ZnO bilayer ETLs and 100 nm Ag top contacts (Figure 6A). As expected, we observed similar results for inverted *p-i-n*-type device configurations. Cross-sectional images of the whole device indicate a perfect desired device configuration. Thick perovskite layers nearly 462 and 510 nm were formed on NiO_x HTLs for control and 1% HEA-based devices, respectively (Figures 6B and 6C). From a cross-sectional view, we can easily distinguish the improved morphology and grain quality for the 1% HEA-based device. We observed well-defined and larger grains, which are completely different from the control device and were grown perpendicular to the FTO substrate. The average thickness of the perovskite layer on the FTO/NiOx HTL improved from 462 to 520 nm after 1% HEA addition. Interestingly, the 1% HEA-based device exhibits slight

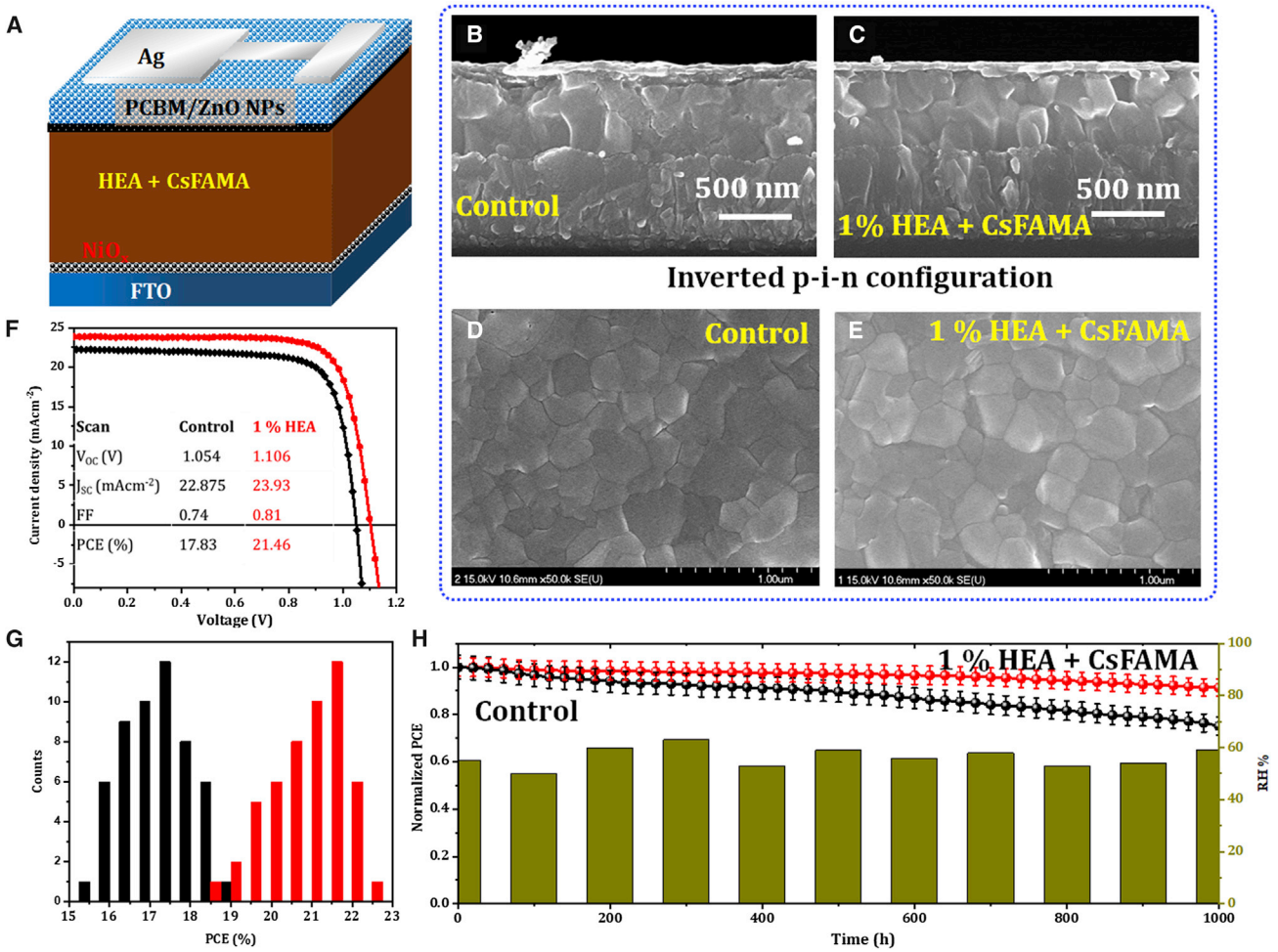

Figure 6. Inverted *p-i-n* device configuration and photovoltaic properties

(A–C) Schematic device configuration (A) and cross-sectional SEM images (B and C) of *p-i-n*-type complete device.

(D and E) SEM images of control and 1% HEA-additive-based samples.

(F) J-V curves for the best-performing devices using perovskite films prepared by using different HEA concentrations measured under standard AM1.5 solar radiation.

(G) The statistics of PCE distribution for 50 devices for each control and 1% HEA-based device.

(H) Photostability recorded under 100 mW cm^{-2} white LED continuous illumination in ambient condition at 85°C thermal stress at 55%–65% RH. Error bar ±5 %. SEM images were recorded using beam intensity 15 kV at 50 k magnification.

improvement in film thickness and reached up to 520 nm. Of note, we observed that the perovskite capping layer of the HEA-based device had more well-defined large grains than the control sample. Furthermore, the perovskite thin films with the 1% HEA additive exhibited improved morphology. From SEM analysis, it is clear that the control sample exhibited a wide range of grain-size distribution, with 185.3 nm average grain size, which improved to 247.47 nm after 1% HEA addition (Figure S25). These results are consistent with our mp-TiO_2 ETL-based perovskite thin films. Figure 6F shows the J-V characteristics of the control and 1% HEA-additive-based *p-i-n* inverted devices. Bare devices fabricated on the NiO_x HTL exhibited a V_{OC} of 1.054 V, a J_{SC} of 22.87 mA cm^{-2}, and an FF of 0.74, yielding 17.83% PCE. As expected, for the 1% HEA addition, we observed substantial improvement in V_{OC} and reached up to 1.107 V with a J_{SC} of 23.93 mA cm^{-2} and an FF of 0.81, yielding 21.46% PCE, which is also competitive as far as the inverted *p-i-n* type is concerned (Table 2). This increment was also observed in our EQE spectra (Figure S26).

Table 2. Photovoltaic performance of inverted NiO_x HTL-based *p-i-n*-type HEA-based perovskite solar cells

Device	V_{OC} (V)	J_{SC} (mA cm^{-2})	FF	PCE (%)
Control	1.054	22.87	0.74	17.83
1% HEA	1.107	23.93	0.81	21.46

Reproducibility histograms of PCE for control and 1% HEA exhibited much better device performance and high reproducibility for HEA-based devices (Figure 6G).

Device stability under thermal stress of the control and HEA-based devices

The long-term stability of HPSCs is one of the key tasks for its on-site application. It is well known that bare $MAPbI_3$ or $FAPbI_3$ is either unstable or shows poor efficiency. This degradation originated from unstable organic cations and their hygroscopic nature. Therefore, mixed-halide-containing Cs-cation (herein, triple-cation) incorporation attracted tremendous interest because of its highly stable and efficient performance. However, defect sites and irregular film growth make them unstable. Therefore, a number of alternative approaches such as passivation of grain boundaries, surface defects, and increase in grain size of the perovskite grain have been adopted in order to make a stable perovskite film. As expected, the *p-i-n* device configuration exhibited much higher stability because of dopant-free HTLs and ETLs (Figure 6H). The photostability of the control CsFAMA-based HPSC device at 85°C thermal stress exhibited ~72% retention of its initial efficiency over 1,000 h. In contrast, 1% HEA-based HPSC devices retaining ~88% of their initial efficiency over 1,000 h exhibit excellent stability against thermal stress for unencapsulated devices. This higher photostability arises from the dual functionality of HEA, such as increased grain size from ~180 nm to 240 nm and defect and surface passivation. Therefore, the degradation at the grain-boundary sites in large-grain films is limited, which improves photostability as well as thermal stability. Besides, increased grain size and defect passivation by HEA facilitates improved moisture stability. Therefore, 1% HEA-based HPSC devices exhibited excellent stability against continuous light illumination, thermal stress, and atmospheric moisture. Furthermore, the metal oxides are thermally stable, with better charge-transport properties. In order to check the phase stability with respect to HEA addition, we monitored the perovskite layer exposed to ambient air and recorded its XRD patterns (Figure S27). After 72 h air exposure, bare perovskite thin films exhibited peak shifts in characteristics at 110 peaks (Figure S27A). In contrast, the XRD patterns of 1% HEA-based thin films exhibited stable peak positions (Figure S27B). These results exhibited that HEA plays a key role in maintaining the perovskite phase in ambient condition.

Long-term stability in air at 85°C up to 200 days has been monitored (Figure S28). For long-term moisture and thermal-stability analysis, we neither used encapsulation nor control humidity conditions. We monitored champion devices under 100 mW cm^{-2} white LED illumination in the ambient condition at 55%–65% RH over 200 days. We determined the shelf lifetime under continuous illumination for control and 1% HEA-based devices. Interestingly, the HEA-based device retained >90% stability over half a year, which is almost 50% higher than the control device. The stability of these perovskite devices is acceptable as per industrial norms and would be suitable for commercialization. We believe that the low-cost HEA-additive-based HPSCs double the long-term stability of the triple-cation perovskite absorber. Our results demonstrated that control HPSCs retain only 45% initial efficiency at 85°C thermal stress. In contrast, the 1% HEA-based device maintains >90% of its initial efficiency over 200 days, which is much higher than bare HPSCs (Figure 6H).

In conclusion, we fabricated high-quality, triple-cation perovskite thin films with a significant increase in grain size through HEA additive. The HEA additive not only influences the crystallization process but also contributes to bulk and surface passivation through O−H and C=O functional groups. The dual functionality of the HEA additive was elucidated by growth mechanism, FT-IR, NMR, and XPS analyses. Our results demonstrated that the HEA additive not only participates in passivation of defect states but also contributes to the crystallization process through the cation-exchange process. With optimized HEA additive concentrations and solvent engineering processes, we achieved more than 22% PCE from a reverse scan for HPSCs. The device fabricated through HEA additives exhibits excellent photostability over 1,000 h under continuous 1 sun equivalent illumination. Our TOF-SIMS investigation revealed that the halide-anion migration is suppressed due to the HEA additive, which facilitates reduced hysteresis and improved stability. This investigation provides a new approach toward high-performance HPSCs having long-term operational stability via a novel dual-functional HEA additive that would be suitable for on-site application.

EXPERIMENTAL PROCEDURES

Resource availability

Lead contact

Further information and requests for resources should be directed to and will be fulfilled by the lead contact, Sawanta S. Mali (sawantasolar@gmail.com, sawanta@jnu.ac.kr) or by Chang Kook Hong (hongck@jnu.ac.kr).

Materials availability

All solvents and reagents were obtained from commercial sources and used without further purification.

Data and code availability

All data supporting the findings of this study are presented within the article and supplemental information. All other data are available from the lead contact upon reasonable request.

Methods

See supplemental experimental procedures for detailed experimental methodology, TRPL analysis by FLIM (Note S1), and single-carrier device analysis (Note S2). Detailed analyses have been given, such as FT-IR, NMR, AFM, PL, FLIM, EDS point mapping, TOF-SIMS, and XRD stability analysis in Figures S1−S28, Notes S1 and S2, and Tables S1−S7.

SUPPLEMENTAL INFORMATION

Supplemental information can be found online at https://doi.org/10.1016/j.xcrp.2022.100906.

ACKNOWLEDGMENTS

This research is supported by the National Research Foundation of Korea (NRF) (2020R1A2C2004880). This work was also supported by Priority Research Centers Program through the National Research Foundation of Korea (NRF), funded by the Ministry of Education, Science and Technology (2018R1A6A1A03024334). This work was also supported by a National Research Foundation of Korea (NRF) grant funded by the Korean government (MSIT) (2018R1C1B6008218). The authors are also thankful to Dr. Julien A. Steele, cMACS, Department of Microbial and Molecular

Systems, KU Leuven, Celestijnenlaan 200F, 3001 Leuven, Belgium, for valuable suggestions during the revision of this manuscript.

AUTHOR CONTRIBUTIONS

S.S.M. and C.K.H. contributed to the conception and design of the experiments. S.S.M. fabricated all devices and conducted most of the characterizations. S.S.M. and J.V.P. measured the J-V curves and UV-vis spectra. S.S.M., D.W.P., and Y.H.J. carried out TOF-SIMS and EDS point mapping. All authors discussed the results and reviewed the manuscript.

DECLARATION OF INTERESTS

The authors declare no competing interests.

Received: October 12, 2021
Revised: April 25, 2022
Accepted: April 29, 2022
Published: May 25, 2022

REFERENCES

1. Kojima, A., Teshima, K., Shirai, Y., and Miyasaka, T. (2009). Organometal halide perovskites as visible-light sensitizers for photovoltaic cells. J. Am. Chem. Soc. *131*, 6050–6051. https://doi.org/10.1021/ja809598r.

2. Jeon, N.J., Na, H., Jung, E.H., Yang, T.-Y., Lee, Y.G., Kim, G., Shin, H.-W., Seok, S.I., Lee, J., and Seo, J. (2018). A fluorene-terminated hole-transporting material for highly efficient and stable perovskite solar cells. Nat. Energy *3*, 682–689.

3. Zhao, D., Chen, C., Wang, C., Junda, M.M., Song, Z., Grice, C.R., Yu, Y., Li, C., Subedi, B., Podraza, N.J., et al. (2018). Efficient two-terminal all-perovskite tandem solar cells enabled by high-quality low-bandgap absorber layers. Nat. Energy *3*, 1093–1100. https://doi.org/10.1038/s41560-018-0278-x.

4. Shi, D., Adinolfi, V., Comin, R., Yuan, M., Alarousu, E., Buin, A., Chen, Y., Hoogland, S., Rothenberger, A., Katsiev, K., et al. (2015). Low trap-state density and long carrier diffusion in organolead trihalide perovskite single crystals. Science *347*, 519–522. https://doi.org/10.1126/science.aaa2725.

5. Yoo, J.J., Seo, G., Chua, M.R., Park, T.G., Lu, Y., Rotermund, F., Kim, Y.-K., Moon, C.S., Jeon, N.J., Correa-Baena, J.-P., et al. (2021). Efficient perovskite solar cells via improved carrier management. Nature *590*, 587–593. https://doi.org/10.1038/s41586-021-03285-w.

6. National Renewable Energy Laboratory (2022). Solar efficiency chart. https://www.nrel.gov/pv/assets/pdfs/best-research-cell-efficiencies-rev220126.pdf.

7. Mali, S.S., Betty, C.A., Patil, P.S., and Hong, C.K. (2017). Synthesis of a nanostructured rutile TiO_2 electron transporting layer via an etching process for efficient perovskite solar cells: impact of the structural and crystalline properties of TiO_2. J. Mater. Chem. A *5*, 12340–12353. https://doi.org/10.1039/c7ta02822a.

8. Mali, S.S., Patil, J.V., Kim, H.J., and Hong, C.K. (2019). Gallium cationic incorporated compact TiO_2 as an efficient electron-transporting layer for stable perovskite solar cells. Matter *1*, 452–464. https://doi.org/10.1016/j.matt.2019.04.001.

9. Hsu, H.L., Chang, C.C., Chen, C.P., Jiang, B.H., Jeng, R.J., and Cheng, C.H. (2015). High-performance and high-durability perovskite photovoltaic devices prepared using ethylammonium iodide as an additive. J. Mater. Chem. A *3*, 9271–9277. https://doi.org/10.1039/c5ta01563d.

10. Mali, S.S., Patil, J.V., and Hong, C.K. (2019). Hot-air-assisted fully air-processed barium incorporated $CsPbI_2Br$ perovskite thin films for highly efficient and stable All-inorganic perovskite solar cells. Nano Lett. *19*, 6213–6220. https://doi.org/10.1021/acs.nanolett.9b02277.

11. Patil, J.V., Mali, S.S., and Hong, C.K. (2020). A-site rubidium cation-incorporated $CsPbI_2Br$ all-inorganic perovskite solar cells exceeding 17% efficiency. Sol. RRL *4*, 2000164. https://doi.org/10.1002/solr.202000164.

12. Prasanna, R., Leijtens, T., Dunfield, S.P., Raiford, J.A., Wolf, E.J., Swifter, S.A., Werner, J., Eperon, G.E., de Paula, C., Palmstrom, A.F., et al. (2019). Design of low bandgap tin–lead halide perovskite solar cells to achieve thermal, atmospheric and operational stability. Nat. Energy *4*, 939–947. https://doi.org/10.1038/s41560-019-0471-6.

13. Yang, F., Hirotani, D., Kapil, G., Kamarudin, M.A., Ng, C.H., Zhang, Y., Shen, Q., and Hayase, S. (2018). All-inorganic $CsPb_{1-x}Ge_xI_2Br$ perovskite with enhanced phase stability and photovoltaic performance. Angew. Chem. Int. Ed. *57*, 12745–12749. https://doi.org/10.1002/anie.201807270.

14. You, J., Hong, Z., Yang, Y.M., Chen, Q., Cai, M., Song, T.-B., Chen, C.-C., Lu, S., Liu, Y., Zhou, H., and Yang, Y. (2014). Low-temperature solution-processed perovskite solar cells with high efficiency and flexibility. ACS Nano *8*, 1674–1680. https://doi.org/10.1021/nn406020d.

15. Mali, S.S., Shim, C.S., and Hong, C.K. (2015). Highly stable and efficient solid-state solar cells based on methylammonium lead bromide ($CH_3NH_3PbBr_3$) perovskite quantum dots. NPG Asia Mater. *7*, e208. https://doi.org/10.1038/am.2015.86.

16. Saliba, M., Matsui, T., Seo, J.Y., Domanski, K., Correa-Baena, J.P., Nazeeruddin, M.K., Zakeeruddin, S.M., Tress, W., Abate, A., Hagfeldt, A., and Gratzel, M. (2016). Cesium containing triple cation perovskite solar cells: improved stability, reproducibility and high efficiency. Energy Environ. Sci. *9*, 1989–1997. https://doi.org/10.1039/c5ee03874j.

17. Patil, J.V., Mali, S.S., and Hong, C.K. (2019). A thiourea additive-based quadruple cation lead halide perovskite with an ultra-large grain size for efficient perovskite solar cells. Nanoscale *11*, 21824–21833. https://doi.org/10.1039/c9nr07377a.

18. Bai, S., Da, P., Li, C., Wang, Z., Yuan, Z., Fu, F., Kawecki, M., Liu, X., Sakai, N., Wang, J.T.W., et al. (2019). Planar perovskite solar cells with long-term stability using ionic liquid additives. Nature *571*, 245–250.

19. Yang, S., Chen, S., Mosconi, E., Fang, Y., Xiao, X., Wang, C., Zhou, Y., Yu, Z., Zhao, J., Gao, Y., et al. (2019). Stabilizing halide perovskite surfaces for solar cell operation with wide-bandgap lead oxysalts. Science *365*, 473–478. https://doi.org/10.1126/science.aax3294.

20. Zheng, X., Zheng, X., Hou, Y., Bao, C., Yin, J., Yuan, F., Huang, Z., Song, K., Liu, J., Troughton, J., et al. (2020). Managing grains and interfaces via ligand anchoring enables 22.3%-efficiency inverted perovskite solar cells. Nat. Energy *5*, 131–140. https://doi.org/10.1038/s41560-019-0538-4.

21. Choi, M.J., Lee, Y.S., Cho, I.H., Kim, S.S., Kim, D.H., Kwon, S.N., and Na, S.I. (2020). Functional additives for high-performance inverted planar

perovskite solar cells with exceeding 20% efficiency: selective complexation of organic cations in precursors. Nano Energy *71*, 104639. https://doi.org/10.1016/j.nanoen.2020.104639.

22. Kang, Y.J., Kwon, S.-N., Cho, S.-P., Seo, Y.H., Choi, M.J., Kim, S.-S., and Na, S.I. (2020). Antisolvent additive engineering containing dual-function additive for triple-cation p–i–n perovskite solar cells with over 20% PCE. ACS Energy Lett. *5*, 2535–2545. https://doi.org/10.1021/acsenergylett.0c01130.

23. Yang, S., Wang, Y., Liu, P., Cheng, Y.B., Zhao, H.J., and Yang, H.G. (2016). Functionalization of perovskite thin films with moisture-tolerant molecules. Nat. Energy *1*, 15016. https://doi.org/10.1038/nenergy.2015.16.

24. Li, X., Ibrahim Dar, M., Yi, C.Y., Luo, J.S., Tschumi, M., Zakeeruddin, S.M., Nazeeruddin, M.K., Han, H.W., and Gratzel, M. (2015). Improved performance and stability of perovskite solar cells by crystal crosslinking with alkylphosphonic acid ω-ammonium chlorides. Nat. Chem. *7*, 703–711. https://doi.org/10.1038/nchem.2324.

25. Mercier, N. (2005). $HO_2C(CH_2)_3NH_3)_2(CH_3NH_3)Pb_2I_7$: a predicted non-centrosymmetrical structure built up from carboxylic acid supramolecular synthons and bilayer perovskite sheets. CrystEngComm *7*, 429–432. https://doi.org/10.1039/b504342e.

26. Li, Y., Zheng, G., and Lin, J. (2008). Synthesis, structure, and optical properties of a contorted <110>-Oriented layered hybrid perovskite: $C_3H_{11}SN_3PbBr_4$. Eur. J. Inorg. Chem. *2008*, 1689–1692. https://doi.org/10.1002/ejic.200700927.

27. Liu, L., Mei, A., Liu, T., Jiang, P., Sheng, Y., Zhang, L., and Han, H. (2015). Fully printable mesoscopic perovskite solar cells with organic silane self-assembled monolayer. J. Am. Chem. Soc. *137*, 1790–1793. https://doi.org/10.1021/ja5125594.

28. Niu, G., Li, W., Meng, F., Wang, L., Dong, H., and Qiu, Y. (2014). Study on the stability of $CH_3NH_3PbI_3$ films and the effect of post-modification by aluminum oxide in all-solid-state hybrid solar cells. J. Mater. Chem. A *2*, 705–710. https://doi.org/10.1039/c3ta13606j.

29. Noel, N.K., Abate, A., Stranks, S.D., Parrott, E.S., Burlakov, V.M., Goriely, A., Noel, N.K., Abate, A., Stranks, S.D., Parrott, E.S., et al. (2014). Enhanced photoluminescence and solar cell performance via Lewis base passivation of organic–inorganic lead halide perovskites. ACS Nano *8*, 9815–9821. https://doi.org/10.1021/nn5036476.

30. Zuo, L., Guo, H., deQuilettes, D.W., Jariwala, S., De Marco, N., Dong, S., DeBlock, R., Ginger, D.S., Dunn, B., Wang, M., and Yang, Y. (2017). Polymer-modified halide perovskite films for efficient and stable planar heterojunction solar cells. Sci. Adv. *3*, e1700106. https://doi.org/10.1126/sciadv.1700106.

31. Liu, L., Fang, W.H., Long, R., and Prezhdo, O.V. (2018). Lewis base passivation of hybrid halide perovskites slows electron–hole recombination: time-domain ab initio analysis. J. Phys. Chem. Lett. *9*, 1164–1171. https://doi.org/10.1021/acs.jpclett.8b00177.

32. Wen, T.Y., Yang, S., Liu, P.F., Tang, L.J., Qiao, H.W., Chen, X., Yang, X.H., Hou, Y., and Yang, H.G. (2018). Surface electronic modification of perovskite thin film with water-resistant electron delocalized molecules for stable and efficient photovoltaics. Adv. Energy Mater. *8*, 1703143. https://doi.org/10.1002/aenm.201703143.

33. Zeng, Q., Zhang, X., Feng, X., Lu, S., Chen, Z., Yong, X., Redfern, S.A.T., Wei, H., Wang, H., Shen, H., et al. (2018). Polymer-passivated inorganic cesium lead mixed-halide perovskites for stable and efficient solar cells with high open-circuit voltage over 1.3 V. Adv. Mater. *30*, 1705393. https://doi.org/10.1002/adma.201705393.

34. Hou, Y., Zhou, Z.R., Wen, T.Y., Qiao, H.W., Lin, Z.Q., Ge, B., and Yang, H.G. (2019). Enhanced moisture stability of metal halide perovskite solar cells based on sulfur–oleylamine surface modification. Nanoscale Horiz. *4*, 208–213. https://doi.org/10.1039/c8nh00163d.

35. Wu, Z., Raga, S.R., Juarez-Perez, E.J., Yao, X., Jiang, Y., Ono, L.K., Ning, Z., Tian, H., and Qi, Y. (2018). Improved efficiency and stability of perovskite solar cells induced by C=O functionalized hydrophobic ammonium-based additives. Adv. Mater. *30*, 1703670. https://doi.org/10.1002/adma.201703670.

36. deQuilettes, D.W., Koch, S., Burke, S., Paranji, R.K., Shropshire, A.J., Ziffer, M.E., and Ginger, D.S. (2016). Photoluminescence lifetimes exceeding 8 μs and quantum yields exceeding 30% in hybrid perovskite thin films by ligand passivation. ACS Energy Lett. *1*, 438–444. https://doi.org/10.1021/acsenergylett.6b00236.

37. Jeon, N.J., Noh, J.H., Kim, Y.C., Yang, W.S., Ryu, S., and Seok, S.I. (2014). Solvent engineering for high-performance inorganic–organic hybrid perovskite solar cells. Nat. Mater. *13*, 897–903. https://doi.org/10.1038/nmat4014.

38. Lin, Y., Shen, L., Dai, J., Deng, Y., Wu, Y., Bai, Y., Zheng, X., Wang, J., Fang, Y., Wei, H., et al. (2017). π-Conjugated Lewis base: efficient trap-passivation and charge-extraction for hybrid perovskite solar cells. Adv. Mater. *29*, 1604545. https://doi.org/10.1002/adma.201604545.

39. Zheng, H., Zhu, L., Hu, L., Yang, S., Chen, S., Alsaedi, A., Hayat, T., Huang, Y., Pan, X., and Dai, S. (2018). Promoting perovskite crystal growth to achieve highly efficient and stable solar cells by introducing acetamide as an additive. J. Mater. Chem. A *6*, 9930–9937. https://doi.org/10.1039/c8ta02121j.

40. Li, W., Dong, H., Guo, X., Li, N., Li, J., Niu, G., and Wang, L. (2014). Graphene oxide as dual functional interface modifier for improving wettability and retarding recombination in hybrid perovskite solar cells. J. Mater. Chem. A *2*, 20105–20111. https://doi.org/10.1039/c4ta05196c.

41. Li, X., Chen, C.-C., Cai, M., Hua, X., Xie, F., Liu, X., Hua, J., Long, Y.-T., Tian, H., and Han, L. (2018). Efficient passivation of hybrid perovskite solar cells using organic dyes with -COOH functional group. Adv. Energy Mater. *8*, 20.

42. Mali, S.S., Patil, J.V., Kim, H.J., Kim, H.H., and Hong, C.K. (2019). A dual-retarded reaction processed mixed-cation perovskite layer for high-efficiency solar cells. Adv. Funct. Mater. *29*, 1807420. https://doi.org/10.1002/adfm.201807420.

43. Chen, B., Rudd, P.N., Yang, S., Yuan, Y., and Huang, J. (2019). Imperfections and their passivation in halide perovskite solar cells. Chem. Soc. Rev. *48*, 3842–3867. https://doi.org/10.1039/c8cs00853a.

44. Tang, G., You, P., Tai, Q., Wu, R., and Yan, F. (2018). Performance enhancement of perovskite solar cells induced by lead acetate as an additive. Sol. RRL *2*, 1800066. https://doi.org/10.1002/solr.201800066.

45. Yang, W.S., Noh, J.H., Jeon, N.J., Kim, Y.C., Ryu, S., Seo, J., and Seok, S.I. (2015). High-performance photovoltaic perovskite layers fabricated through intramolecular exchange. Science *348*, 1234–1237. https://doi.org/10.1126/science.aaa9272.

46. Wang, S., Ma, Z., Liu, B., Wu, W., Zhu, Y., Ma, R., and Wang, C. (2018). High-performance perovskite solar cells with large grain-size obtained by using the Lewis acid-base adduct of thiourea. Sol. RRL *2*, 1800034. https://doi.org/10.1002/solr.201800034.

47. Aharon, S., Dymshits, A., Rotem, A., and Etgar, L. (2015). Temperature dependence of hole conductor free formamidinium lead iodide perovskite based solar cells. J. Mater. Chem. A *3*, 9171–9178. https://doi.org/10.1039/c4ta05149a.

48. Pont, S., Bryant, D., Lin, C.-T., Aristidou, N., Wheeler, S., Ma, X., Godin, R., Haque, S.A., and Durrant, J.R. (2017). Tuning $CH_3NH_3Pb(I_{1-x}Br_x)_3$ perovskite oxygen stability in thin films and solar cells. J. Mater. Chem. A *5*, 9553–9560. https://doi.org/10.1039/c7ta00058h.

49. Li, N., Tao, S., Chen, Y., Niu, X., Onwudinanti, C.K., Hu, C., Qiu, Z., Xu, Z., Zheng, G., Wang, L., et al. (2019). Cation and anion immobilization through chemical bonding enhancement with fluorides for stable halide perovskite solar cells. Nat. Energy *4*, 408–415. https://doi.org/10.1038/s41560-019-0382-6.

50. Braunger, S., Mundt, L.E., Wolff, C.M., Mews, M., Rehermann, C., Jošt, M., Tejada, A., Eisenhauer, D., Becker, C., Guerra, J.A., et al. (2018). $Cs_xFA_{1-x}Pb(I_{1-y}Br_y)_3$ perovskite compositions: the ppearance of wrinkled morphology and its impact on solar cell performance. J. Phys. Chem. C *122*, 17123–17135. https://doi.org/10.1021/acs.jpcc.8b06459.

51. Liu, C., Li, W., Li, H., Wang, H., Zhang, C., Yang, Y., Gao, X., Xue, Q., Yip, H.-L., Fan, J., et al. (2019). Structurally reconstructed $CsPbI_2Br$ perovskite for highly stable and square-centimeter all-inorganic perovskite solar cells. Adv. Energy Mater. *9*, 1803572. https://doi.org/10.1002/aenm.201803572.

52. Moulder, J.F., Stickle, W.F., Sobol, P.E., and Bomben, K.D. (1992). Handbook of X-Ray Photoelectron Spectroscopy: A Reference Book of Standard Spectra for Identification and Interpretation of XPS Data (Perkin-Elmer).

53. Dong, X., Chen, D., Zhou, J., Zheng, Y.Z., and Tao, X. (2018). High crystallization of a multiple cation perovskite absorber for low-temperature stable ZnO solar cells with high-efficiency of over 20%. Nanoscale *10*, 7218–7227. https://doi.org/10.1039/c8nr00152a.

54. Zhu, K., Cong, S., Lu, Z., Lou, Y., He, L., Li, J., Ding, J., Yuang, N., Rümmeli, M.H., and Zou, G.J. (2019). Enhanced perovskite solar cell performance via defect passivation with ethylamine alcohol chlorides additive. J. Power Sources *428*, 82–87. https://doi.org/10.1016/j.jpowsour.2019.04.056.

55. Jiang, H., Yan, Z., Zhao, H., Yuan, S., Yang, Z., Li, J., Liu, B., Niu, T., Feng, J., Wang, Q., et al. (2018). Bifunctional hydroxylamine hydrochloride incorporated perovskite films for efficient and stable planar perovskite solar cells. ACS Appl. Energy Mater. *1*, 900–909. https://doi.org/10.1021/acsaem.8b00060.

56. Luo, D., Yang, W., Wang, Z., Sadhanala, A., Hu, Q., Su, R., Shivanna, R., Trindade, G.F., Watts, J.F., Xu, Z., et al. (2018). Enhanced photovoltage for inverted planar heterojunction perovskite solar cells. Science *360*, 1442–1446. https://doi.org/10.1126/science.aap9282.

57. Quarti, C., De Angelis, F.D., and Beljonne, D. (2017). Influence of surface termination on the energy level alignment at the $CH_3NH_3PbI_3$ perovskite/C_{60} interface. Chem. Mater. *29*, 958–968. https://doi.org/10.1021/acs.chemmater.6b03259.

58. Stranks, S.D., Burlakov, V.M., Leijtens, T., Ball, J.M., Goriely, A., and Snaith, H.J. (2014). Recombination kinetics in organic-inorganic perovskites: excitons, free charge, and subgap states. Phys. Rev. Appl. *2*, 034007. https://doi.org/10.1103/physrevapplied.2.034007.

59. Habisreutinger, S.N., Noel, N.K., Snaith, H.J., and Nicholas, R.J. (2017). Investigating the role of 4-tert butylpyridine in perovskite solar cells. Adv. Energy Mater. *7*, 1601079. https://doi.org/10.1002/aenm.201601079.

60. Li, X., Bi, D., Yi, C., Décoppet, J.-D., Luo, J., Zakeeruddin, S.M., Hagfeldt, A., and Grätzel, M. (2016). A vacuum flash–assisted solution process for high-efficiency large-area perovskite solar cells. Science *353*, 58–62. https://doi.org/10.1126/science.aaf8060.

61. Liu, C., Cheng, Y.B., and Ge, Z. (2020). Understanding of perovskite crystal growth and film formation in scalable deposition processes. Chem. Soc. Rev. *49*, 1653–1687. https://doi.org/10.1039/c9cs00711c.

62. Lakowicz, J.R. (2006). Principles of Flurescence Spectroscopy, Third edition (Springer).

63. Sillen, A., and Engelborghs, Y. (1998). The correct use of "average" fluorescence parameters. Photochem. Photobiol. *67*, 475. https://doi.org/10.1562/0031-8655(1998)067<0475:tcuofp>2.3.co;2.

64. deQuilettes, D.W., Zhang, W., Burlakov, V.M., Graham, D.J., Leijtens, T., Osherov, A., Bulović, V., Snaith, H.J., Ginger, D.S., and Stranks, S.D. (2016). Photo-induced halide redistribution in organic–inorganic perovskite films. Nat. Commun. *7*, 11683. https://doi.org/10.1038/ncomms11683.

65. Snaith, H.J., Abate, A., Ball, J.M., Eperon, G.E., Leijtens, T., Noel, N.K., Stranks, S.D., Wang, J.T.-W., Wojciechowski, K., and Zhang, W. (2014). Anomalous hysteresis in perovskite solar cells. J. Phys. Chem. Lett. *5*, 1511–1515. https://doi.org/10.1021/jz500113x.

66. Li, W., Zhang, W., Van Reenen, S., Sutton, R.J., Fan, J., Haghighirad, A.A., Johnston, M.B., Wang, L., and Snaith, H.J. (2016). Enhanced UV-light stability of planar heterojunction perovskite solar cells with caesium bromide interface modification. Energy Environ. Sci. *9*, 490–498. https://doi.org/10.1039/c5ee03522h.

67. Shao, Y., Xiao, Z., Bi, C., Yuan, Y., and Huang, J. (2014). Origin and elimination of photocurrent hysteresis by fullerene passivation in $CH_3NH_3PbI_3$ planar heterojunction solar cells. Nat. Commun. *5*, 5784. https://doi.org/10.1038/ncomms6784.

68. Wang, Z., Lin, Q., Chmiel, F.P., Sakai, N., Herz, L.M., and Snaith, H.J. (2017). Efficient ambient-air-stable solar cells with 2D–3D heterostructured butylammonium-caesium-formamidinium lead halide perovskites. Nat. Energy *2*, 17135. https://doi.org/10.1038/nenergy.2017.135.

69. Wang, K., Shi, Y., Li, B., Zhao, L., Wang, W., Wang, X., Bai, X., Wang, S., Hao, C., Wang, K., et al. (2016). Amorphous inorganic electron-selective layers for efficient perovskite solar cells: feasible strategy towards room-temperature fabrication. Adv. Mater. *28*, 1891–1897. https://doi.org/10.1002/adma.201505241.

70. Shuttle, C.G., O'Regan, B., Ballantyne, A.M., Nelson, J., Bradley, D.D.C., and Durrant, J.R. (2008). Bimolecular recombination losses in polythiophene: fullerene solar cells. Phys. Rev. B *78*, 113201. https://doi.org/10.1103/physrevb.78.113201.

71. Proctor, C.M., Kuik, M., and Nguyen, T.-Q. (2013). Charge carrier recombination in organic solar cells. Prog. Polym. Sci. *38*, 1941–1960. https://doi.org/10.1016/j.progpolymsci.2013.08.008.

72. Wang, H., Hsu, J.-H., Yang, G., and Yu, C. (2016). Novel organic Schottky barrier diode created in a single planar polymer film. Adv. Mater. *28*, 9545–9549. https://doi.org/10.1002/adma.201602930.

73. Tan, H., Jain, A., Voznyy, O., Lan, X., Garcıa de Arquer, F.P., Fan, J.Z., Quintero-Bermudez, R., Yuan, M., Zhang, B., Zhao, Y., et al. (2017). Efficient and stable solution-processed planar perovskite solar cells viacontact passivation. Science *355*, 722–726. https://doi.org/10.1126/science.aai9081.

74. Galkowski, K., Mitioglu, A., Miyata, A., Plochocka, P., Portugall, O., Eperon, G.E., Wang, J.T.W., Stergiopoulos, T., Stranks, S.D., Snaith, H.J., and Nicholas, R.J. (2016). Determination of the exciton binding energy and effective masses for methylammonium and formamidinium lead tri-halide perovskite semiconductors. Energy Environ. Sci. *9*, 962–970. https://doi.org/10.1039/c5ee03435c.

75. Xu, Z., Wu, J., Yang, Y., Lan, Z., and Lin, J. (2018). High-efficiency planar hybrid perovskite solar cells using indium sulfide as electron transport layer. ACS Appl. Energy Mater. *1*, 4050–4056. https://doi.org/10.1021/acsaem.8b00726.

76. Wu, X., Li, H., Wang, K., Sun, X., and Wang, L. (2018). $CH_3NH_3Pb_{1-x}Eu_xI_3$ mixed halide perovskite for hybrid solar cells: the impact of divalent europium doping on efficiency and stability. RSC Adv. *8*, 11095–11101. https://doi.org/10.1039/c7ra12754e.

77. Luo, D., Zhao, L., Wu, J., Hu, Q., Zhang, Y., Xu, Z., Liu, Y., Liu, T., Chen, K., Yang, W., et al. (2017). Dual-source precursor approach for highly efficient inverted planar heterojunction perovskite solar cells. Adv. Mater. *29*, 1604758. https://doi.org/10.1002/adma.201604758.

78. Domanski, K., Correa-Baena, J.-P., Mine, N., Nazeeruddin, M.K., Abate, A., Saliba, M., Tress, W., Hagfeldt, A., and Grätzel, M. (2016). Not all that glitters is gold: metal-migration-induced degradation in perovskite solar cells. ACS Nano *10*, 6306–6314. https://doi.org/10.1021/acsnano.6b02613.

79. Shao, Y., Fang, Y., Li, T., Wang, Q., Dong, Q., Deng, Y., Yuan, Y., Wei, H., Wang, M., Gruverman, A., et al. (2016). Grain boundary dominated ion migration in polycrystalline organic–inorganic halide perovskite films. Energy Environ. Sci. *9*, 1752–1759. https://doi.org/10.1039/c6ee00413j.

80. Li, Z., Xiao, C., Yang, Y., Harvey, S.P., Kim, D.H., Christians, J.A., Yang, M., Schulz, P., Nanayakkara, S.U., Jiang, C.S., et al. (2017). Extrinsic ion migration in perovskite solar cells. Energy Environ. Sci. *10*, 1234–1242. https://doi.org/10.1039/c7ee00358g.

81. Zhang, T., Meng, X., Bai, Y., Xiao, S., Hu, C., Yang, Y., Chen, H., and Yang, S. (2017). Profiling the organic cation-dependent degradation of organolead halide perovskite solar cells. J. Mater. Chem. A *5*, 1103–1111. https://doi.org/10.1039/c6ta09687e.

82. Mali, S.S., Kim, H.J., Kim, H.H., Shim, S.E., and Hong, C.K. (2018). Nanoporous p-type NiOx electrode for p-i-n inverted perovskite solar cell toward air stability. Mater. Today *21*, 483–500. https://doi.org/10.1016/j.mattod.2017.12.002.

83. Mali, S.S., Patil, J.V., Kim, H.J., Luque, R., and Hong, C.K. (2019). Highly efficient thermally stable perovskite solar cells via Cs:NiO_x/CuSCN double-inorganic hole extraction layer interface engineering. Mater. Today *26*, 8–18. https://doi.org/10.1016/j.mattod.2019.01.017.

84. Christians, J.A., Schulz, P., Tinkham, J.S., Schloemer, T.H., Harvey, S.P., Tremolet de Villers, B.J., Sellinger, A., Berry, J.J., and Luther, J.M. (2018). Tailored interfaces of unencapsulated perovskite solar cells for >1,000 hour operational stability. Nat. Energy *3*, 68–74. https://doi.org/10.1038/s41560-017-0067-y.